Design, construction and test of the primary target system for $\overline{\text{P}}$ANDA

Marta Martínez Rojo

Institut für Kernphysik

Johannes Gutenberg-Universität Mainz

Betreut durch Prof. Dr. Josef Pochodzalla

Januar 2016

Eidesstattliche Erklärung

Hiermit versichere ich, die vorliegende Arbeit selbstständig und unter ausschließlicher Verwendung der angegebenen Literatur und Hilfsmittel erstellt zu haben.

Die Arbeit wurde bisher in gleicher oder ähnlicher Form keiner anderen Prüfungsbehörde vorgelegt und auch nicht veröffentlicht.

Marta Martinez Rojo

Contents

Introduction

The advent of new accelerator technologies, like the use of intense and stored anti-proton beams, will set an inflection point in what we know today as Modern Physics. In particular, the $\overline{\text{P}}$ANDA experiment at the FAIR facility in Darmstadt (Germany) will help to elucidate many of the still obscure aspects of the strong interaction and, consequently, build a bridge between nuclear and hadron physics. Hypernuclear physics is currently attracting a renewed attention. This is mainly due to the important role of hypernuclei spectroscopy (hyperon-hyperon and hyperon-nucleon interactions) as a unique tool to describe the baryon-baryon interactions in a unified way and to understand the origin of their short-range.

Hypernuclear research will be one of the main topics addressed by the $\overline{\text{P}}$ANDA experiment at the planned Facility for Antiproton and Ion Research FAIR. The FAIR complex will include the High Energy Storage Ring (HESR) to store anti-protons between 0.8 and 14.4 MeV energy. Intense and high quality beams with luminosities up to 10^{32} cm^{-2}s^{-1} and momentum resolutions down to 10^{-5} are expected. The $\overline{\text{P}}$ANDA hypernuclear program shall reveal the strength of Λ–Λ interaction via the high resolution γ-spectroscopy of double Λ hypernuclei. Thanks to the use of stored $\overline{p}$ beams, a copious production of double Λ hypernuclei is expected at the $\overline{\text{P}}$ANDA experiment which will enable high precision γ-spectroscopy of such nuclei for the first time. Hereon the production of low momentum Ξ^- hyperons and their capture in atomic levels is therefore essential for the experiment. Due to the complexity of the production mechanism a devoted target system based on two-interaction points is mandatory. In particular, the aim of this work is to study the feasibility of constructing an operational device capable of dealing with the first step in the hypernuclei production at $\overline{\text{P}}$ANDA. These activities consider

the design and the operational performance of such an apparatus under extreme conditions at the interior of the $\overline{\mathrm{P}}$ANDA spectrometer.

Chapter 1 deals with the fundamentals of Λ–hypernuclear physics: topics like the different hypernuclei production mechanisms, their discovery thanks to nuclear emulsions, the current knowledge on single and double Λ-hypernuclei and the present experimental detection techniques. The characteristics of the High Energy Storage Ring (HESR) that provides the antiprotons for the production of $\Lambda\Lambda$-hypernuclei will be mentioned in chapter 2. Furthermore, the different parts that compose the $\overline{\mathrm{P}}$ANDA spectrometer as well as the operating conditions of the experiment will also be described. In addition, the steps followed at $\overline{\mathrm{P}}$ANDA for the generation of $\Lambda\Lambda$-hypernuclei will be introduced in this chapter.

It is essential for this project to set the requirements that must be taken into account for the selection of an appropriate primary target for the experiment as well as the studies carried out on possible target materials. The feasibility activities considering the operation of a diamond filament target prototype in a large hadronic environment as well as the radiation damages produced after being irradiated will be shown in chapter 3. In chapter 4 the design of a devoted chamber for the primary target will be introduced. In the present design the beam line is surrounded by a window material that can be bent to the inside of the chamber when it is pumped. Therefore, a study of the deformation of the target chamber for different window foils and number of pumping cycles has been carried out. These results will be presented as well.

Consequently, a system that permits to steer the primary target to the primary interaction point and replace it in case of damage is needed. In chapter 5 the different components of such a setup and the procedure followed to arrange all the parts together and operate the system will be commented. Furthermore, it is equally important to describe the tests performed on the motors that carry the target and the calibration method used for the right alignment of the position sensor in the setup. To conclude, chapter 6 includes a brief summary of all the topics

which have been considered for the successful performance of a hypernuclear primary target system at the $\overline{\mathrm{P}}$ANDA experiment. Further improvements of the present design have also been shortly addressed.

1 Hypernuclear Physics

A Λ hyperon is formed by three quarks: up, down and strange $[uds]$ and has a mass $m_\Lambda = 1116$ MeV/c^2 and a mean lifetime $\tau_\Lambda = 2.6 \times 10^{-10}$ s [1]. Because of their long lifetime, hyperons can be bound in nuclei forming the so called hypernuclei. A hyperon bound in a nucleus offers a selective probe of the hadronic many-body problem as it is not restricted by the Pauli principle in populating all possible nuclear states due to the strangeness of the hyperon. That gives it one degree of freedom more and makes it distinguishable from the nucleons. On one hand, a strange baryon embedded in a nuclear system may serve as a sensitive probe for the nuclear structure and its possible modification due to the presence of the hyperon. On the other hand, properties of hyperons may change if implanted inside of a nucleus. Therefore a nucleus may serve as a laboratory offering a unique possibility to study basic properties of hyperons. Thus, hypernuclear physics represents an interdisciplinary science linking many fields of particle, nuclear and many-body physics [2].

Hypernuclei are denoted with the notation $^{A+Y}_{Y}Z$, where Z accounts for the number of protons, A represents the total numbers of nucleons (protons and neutrons) and Y is the number of hyperons. Nuclei with strangeness can be plotted in the three-dimensional nuclear chart, where the strangeness content (S) increases along the third axis. Experimental data are limited to only about 40 different Λ-hypernuclei in the S = -1 plane (blue symbols) and a few $\Lambda\Lambda$-hypernuclei (yellow symbols) in the S = -2 plane (see figure 1.1). Due to experimental limitations the third dimension has only scarcely been explored in the past despite the fact that single and double Λ-hypernuclei were discovered 50 and 40 years ago, respectively [3].

The $\overline{\text{P}}$ANDA hypernuclear program shall reveal the strength of Λ-Λ interaction via the high resolution γ-spectroscopy of double Λ-hypernuclei [4]. Contrary to past hypernuclear experiments, where only a very few double hypernuclei events were found (see table 1.1), the challenge of the $\overline{\text{P}}$ANDA experiment will be to produce statistics of five orders of magnitude larger.
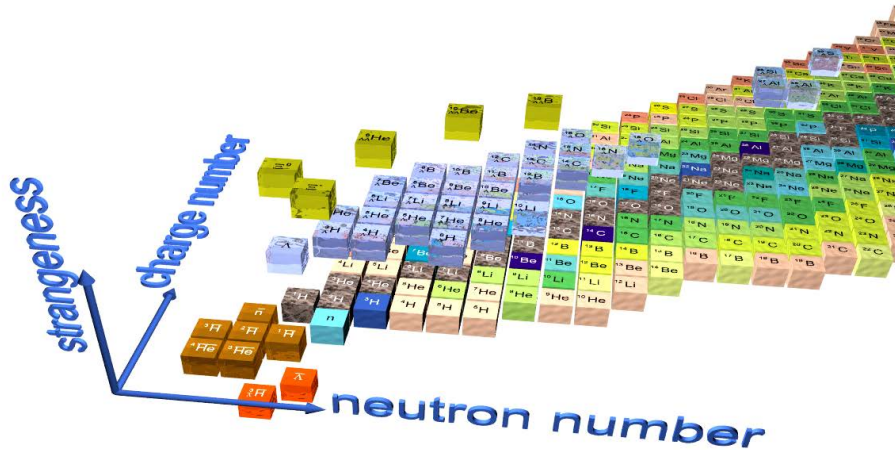

Figure 1.1: Low mass region of 3-dimensional nuclear chart with presently known nuclei, antinuclei, hypernuclei and antihypernuclei.

1.1 Production of hypernuclei

In general, the hypernuclei production is based on the following process,

$$aN \rightarrow Yb \tag{1.1}$$

where a is the projectile interacting with a nucleon N to produce a hyperon Y and a residual particle(s) b. One can distinguish between two categories of reactions to produce, identify and extract properties of hypernuclei. One that relies on the detection of the decay products and another one that employs kinematic information of the production process to identify the produced hypernucleus.

On one hand, hypernuclei can be formed as secondary particles emerging from more or less violent hadronic interactions. The formation of a hypernucleus is tagged by its delayed weak decay producing a secondary vertex. According to Cheston and Primakoff [5], a V-particle bound within a nucleus may decay either by normal mesonic decays $V \to p + \pi^- + 37 MeV$ or $V \to n + \pi^0 + 40 MeV$ or by the interaction with other nucleons of the nucleus changing into a nucleon via $\Lambda + p \to n + p$ or $\Lambda + n \to n + n$ and releasing an energy of approximately 175 MeV. Spectroscopic information is obtained exclusively by analysing the decay products. Examples are cosmic rays interactions in cloud chambers or in emulsions (figure 1.2), the production of single hypernuclei in proton or heavy ion induced reactions or the formation of double hypernuclei after a conversion of a Ξ-hyperon into two Λ-particles. Observables are the binding energies of hypernuclear ground states from the energies and momenta of the decay products, their lifetime by decay in flight and the ratio between the non-mesonic and the mesonic decay probability.

On the other hand, by employing the production kinematics, ground and excited hypernuclear states can be identified by a missing-mass analysis of the incident beam and the associated meson. First experiments concentrated on the (K$^-$, π^-) by making use of K$^-$ mesons at rest in nuclear emulsions. By measuring the momenta of the associated pion, the binding energy of the produced hypernucleus could be inferred. Later, this kinematic method was proposed also for other quasi two-body reactions [6]. Examples are the (π^+, K$^+$) reactions [7] which convert a neutron into a Λ hyperon, the (γ, K$^+$) [8, 9] and (e, e'K$^+$) [8, 10] reactions which convert a proton into a hyperon and the double charge exchange reaction (π^-, K$^+$).
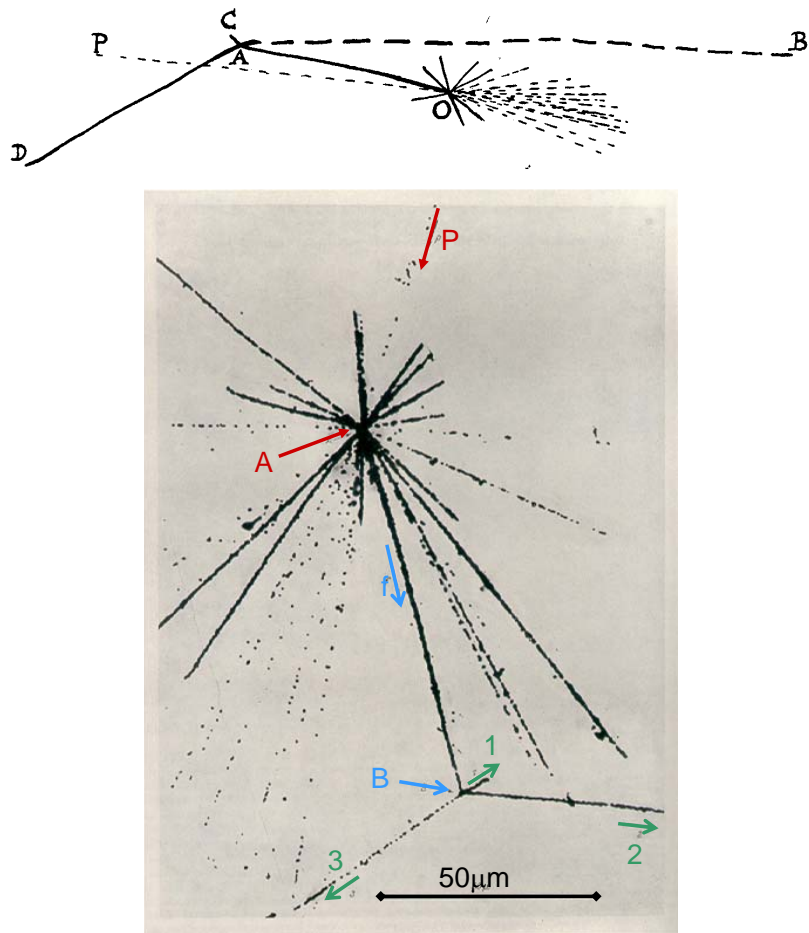
Figure 1.2: The first hyperfragment events seen in nuclear emulsion. The top plot shows the drawing of an event published by Crussard and D. Morellet in January 1953 [11]. The lower plot shows an event submitted by Danysz and Pniewski in december 1952 and published in march 1953. In this picture an incident cosmic ray *P* interacts at *A* with a heavy nucleus in the nuclear emulsion. A produced hyperfragment *f* decays at *B* into three charged particles [12].

Modern experiments making use of electronic detection systems combine information of the production kinematics and the decay products or make use of several decay characteristics. Examples are the high resolution γ-ray spectroscopy of hypernuclei, where the candidates are selected either by two-body kinematics or the weak decay products. The same holds for the hypernuclei experiment at $\bar{\text{P}}$ANDA.

1.2 Discovery of hypernuclei: the emulsion era

Since until now double hypernuclei were produced exclusively in emulsions, in this section the emulsion results will be described in more detail. Concerning nuclei with multiple strangeness, nuclear emulsions are at present still the only source of experimental information. Also for single hypernuclei, emulsion studies still play an important role for our understanding of hypernuclei.

Progress in hypernuclear physics was and is driven by advances in detector technologies. The story of hypernuclear physics began in 1953 when Crussard and Morellet [11], Danysz and Pniewski [12] and Tidman and co-workers [13] discovered nearly simultaneously unusual events, so called connected stars in photographic emulsions. The photographic emulsion technique is based on the usual photo-plates, like those used by Röntgen and Becquerel. The emulsion is thicker and has a high concentration of silver bromide grains that condense along the tracks of particles that pass through the emulsion. Microscopic examination of the properties of the grains that form a particle track gives information about the mass of the particle. The standard products available in the 1930s could only detect slow protons and alpha particles. In the mid-1940s Cecil Frank Powell developed the method of direct registration of charged particle tracks in photographic emulsion into a precision tool for particle physics [14, 15]. From then on the method was successfully used for investigating the properties of muons and pions that were contained in cosmic rays and the detection of more particles that until then were unknown, like the tauon, the kaon and others.

The event that Danysz and Pniewski observed (lower part in figure 1.2), shows a nuclear fragment emerging from a cosmic-ray star that was stopped within the emulsion in about 10^{-12} s and subsequently disintegrated with an energy release of 140 to 180 MeV (figure 1.2). Since the mean life for the emission of a nucleon from a fragment having an excitation energy

around 100 MeV is of the order of 10^{-20} s, a decay of an excited ordinary nucleus was excluded. The fact that the fragment was practically at rest at the moment of its disintegration also excluded the possibility of a secondary collision between f and a nucleus in the emulsion. Due to the time-integrating property of emulsion stacks (see an early discussion in [16]) a chance coincidence of two interactions was considered not to be impossible. However, Tidman and co-workers [13] and also Ciok and co-workers [17] discarded this solution because of the extremely small probability of a repeated chance coincidence [11, 12, 13].

Two possible explanations remained still: (i) a subsequent capture of a π^- meson or some other heavy meson close to the stopping point B in figure 1.2 from an atomic orbit or (ii) a heavy neutral V_1^0-particle -which had been observed only a few years before [18]- in a bound state *within* a nucleus [12]. One of the fragments in the event of Crussard and Morellet turned out to be a pion [11]. As a consequence, a pionic atom as the origin of these connected stars could be discarded. Analysing a two-body decay of a secondary star, Bonetti and co-workers also excluded a capture of a heavier meson as the trigger of the secondary decay [19] leaving only possibility (ii). As suggested by Goldhaber [20] such fragments were called later hyperfragments.

During the first two decades, nuclear emulsions stayed the main source of information on hypernuclei although some important results - mainly on in-flight decays - were also obtained from bubble chambers (see e.g. [21]). Emulsion plates were exposed not only to cosmic rays but more and more to hadron beams at accelerators like proton and pion beams at the Brookhaven cosmotron [20]. Stars caused by stopped Σ^- that were produced in K^- interactions were analyzed as well [22]. The drawbacks of the cosmic ray, proton or pion induced reactions are the large momentum transfer to the hyperon and thus the small probability to form a hypernucleus [23]. On the other hand, for K^--mesons stopped in a nuclear emulsion more observable hypernuclei are produced [24]. As a consequence of the high formation probability, stopped K^--meson interactions as well as K^- interactions in flight became the main source of hypernuclei, both at the Berkeley Bevatron accelerator (see e.g. [25, 26, 27, 28, 29, 30, 31])

and at the CERN-PS (e.g. [32, 33]) in the 1960's.

The binding energy B_Λ of a Λ-hyperon in a hypernucleus is defined by the equation

$$B_\Lambda = (M_{core} + M_{Lambda} - M_{hn})c^2, \tag{1.2}$$

where M_{core}, M_{Lambda} and M_{hn} are the masses of the nuclear core at its ground state, of the Λ-hyperon and of the hypernucleus, respectively. The mass of the hypernucleus M_{hn} can be determined from the sum of the masses m_i of all decay products and their summed kinetic energies T_i:

$$M_{hn} = \sum m_1 c^2 + \sum T_i. \tag{1.3}$$

The most reliable information on B_Λ from emulsion studies resulted from π^--mesonic decays of light s- and p-shell hypernuclei with masses $A \leq 14$ [34, 35, 36, 37, 38]. In such decays the energy release is typically about 30 MeV. Because of this small value, neutron emission is less likely and the probability to stop and identify all decay products is rather high. Having a range in nuclear emulsion between about 13 and 33 mm (see e.g. [39]), at least one particle -the negative pion- is easily identified. On the other hand, π^0-mesons cannot be seen in emulsions and non-mesonic decays involve larger energy releases of around 170 MeV. Particularly, for heavier nuclei this gives usually rise to a disintegration of the nuclear core and multiple neutron emission. But, even for π^- mesonic decays, only the π^- is readily identified. The measured track lengths and the ionization densities are usually not sufficient to uniquely identify the other particles. An unambiguous identification of a hypernucleus is obtained if exactly one permutation of the identities of all decay products fulfills the momentum and energy balance (see e.g. [28]).

Despite the great success of emulsion studies the drawback of the emulsion technique became more and more clear: the tedious and time consuming analysis of the emulsion stacks and, consequently, the very limited statistics (limited species of hypernuclei can be produced by the target nuclei contained in emulsions), and the fact that it is -except of very few exceptions [40, 41]- limited to binding energies of ground states.

1.3 Production of double hypernuclei

The simultaneous production and implantation of two individual Λ's in a nucleus in two distinct processes is not feasible. It is one of the lucky coincidences in physics that the conversion of a Ξ^- and a proton into two Λ's releases –ignoring binding energy effects– only 28 MeV of excitation energy. Because of this low value there is a chance of typically a few percent that both created Λ-hyperons stick to the same nucleus [42, 43, 44].

Unfortunately, Ξ^- hyperons produced in reactions with *conventional* hadron beams have usually rather high momenta. The capture of the Ξ^- in the same nucleus where it has been produced is therefore rather unlikely. Therefore the capture of Ξ-hyperons proceeds usually in two (or even three) steps. Using energetic hadronic beams, a Ξ^- (together with its associated strange particles) is produced in a primary target. In a second step, this Ξ^- is slowed down in a dense, solid material (e.g. a nuclear emulsion) and forms a Ξ^--atom [45]. After an atomic cascade the hyperon is finally captured in the secondary target nucleus. In order to reach a high capture probability it is mandatory to keep the primary momentum of the produced Ξ^- as low as possible. If its momentum is too high, its stopping time will exceed the lifetime and hence the Ξ^- will decay prior to the atomic capture with high probability.

Using the (K^+, K^-) double strangeness exchange reaction, Ξ^-'s are produced with typical momenta of $\sim$500 MeV/c [46, 47]. While most ($\sim$80%) of the Ξ^-'s escape from the target nucleus, in a few percent of the reactions the Ξ-hyperon is captured in the nucleus. The main advantage of this reaction is the fact that the outgoing K^- can be used as a tag for this reaction. The main drawback, however, is the low kaon beam intensity because of its low lifetime and hence the need for thick secondary targets. At this point, it is interesting to note that the $\overline{\Xi}$ was discovered in antiproton-proton interactions at 3 GeV/c [48]. Indeed, relative low momentum Ξ^-'s can also be produced in the $\overline{p} + p \rightarrow \Xi^- + \overline{\Xi}^+$ reaction as will be outlined below. Again,

the $\overline{\Xi}$ can be used as a tag of this reaction. The main advantage compared to the kaon induced reaction is the fact that the anti-proton is stable and can thus be retained in a storage ring. This allows to achieve rather high luminosities even with very thin primary targets.

Because of this two-step process it is not possible to perform spectroscopic studies based on the analysis of two-body reactions like in single hypernuclei reactions. Spectroscopic information on double hypernuclei can only be obtained via their decay. We can distinguish two different steps of the decay process: (i) γ-rays emitted via the sequential decay of an excited double hypernucleus will provide information on the level structure with rather high resolution. (ii) Once that the ground state is reached, the weak decay of the hyperon(s) will initiate the emission of several particles. Here the determination of the ground state mass requires the knowledge of all masses of the various decay products and their kinetic energies. Hence unique identification of the final particles and precise determination of their kinetic energies is mandatory. Nuclear emulsions are even today the only technique which meets all requirements for these measurements of ground state masses. It is however impossible to detect neutrons or γ-rays from intermediate particle unstable fragments with this method. As a consequence, the determination of the ground state mass of double hypernuclei is limited to light nuclei which decay exclusively into charged particles. (iii) Finally, the kinetic energies of weak decay products are also sensitive to the binding energies of the two Λ-hyperons.

1.3.1 Status of identified $\Lambda\Lambda$-hypernuclei

The world supply of data on $\Lambda\Lambda$-hypernuclei is very limited. Until recently only three candidates for double hypernuclei were observed via their double pion decay [49, 50, 51, 52]. In addition, Aoki *et al.* presented evidence of the production and subsequent weak decay of three heavy double hypernuclei [53]. Only lately two additional events were completely identified by the KEK-E373 collaboration which collected approximately 1000 stopped Ξ^-'s [54].

Generally, the Λ-Λ interaction energy, $\Delta B_{\Lambda\Lambda}({}^A_{\Lambda\Lambda}Z)$, of a double hypernucleus with baryon

number A and proton number Z is defined as

$$\Delta B_{\Lambda\Lambda}(^A_{\Lambda\Lambda}Z) = B_\Lambda(^A_{\Lambda\Lambda}Z) - B_\Lambda(^{A-1}_\Lambda Z), \tag{1.4}$$

Of course, this only presents the net Λ-Λ binding provided that the core is not distorted by adding one Λ after the other and that the core spin is zero. The determination of $\Delta B_{\Lambda\Lambda}(^A_{\Lambda\Lambda}Z)$ requires the knowledge of all the masses of the various decay products and their kinetic energies. The deduced values are also sensitive to the population of γ-unstable excited states in the primary $\Lambda\Lambda$-nucleus or its decay products. Table 1.1 summarizes our present knowledge on $\Delta B_{\Lambda\Lambda}(^A_{\Lambda\Lambda}Z)$. Obviously, even the high precision of the emulsion data does not allow an unequivocal interpretation of the deduced values for Λ-Λ in terms of the strength of the Λ-Λ interaction. This difficulty is due to several effects: (i) the dynamical change of the core nucleus [55], (ii) the non-zero spin of the core, (iii) $\Lambda\Lambda - \Xi N$ coupling effects [56] and (iv) the possible production of the hypernuclei in γ-unstable excited states or the emission of undetected neutrons [57].

Nucleus	$\Delta B_{\Lambda\Lambda}(^A_{\Lambda\Lambda}Z)$ (MeV)	Reference
$^6_{\Lambda\Lambda}$He	4.7 ± 0.6	Prowse (1966) [50]
$^6_{\Lambda\Lambda}$He	$1.01 \pm 0.20^{+0.18}_{-0.11}$	KEK-E373 (2001) [53, 54]
$^{10}_{\Lambda\Lambda}$Be	4.3 ± 0.4	Danysz (1963) [49]
$^{10}_{\Lambda\Lambda}$Be	-4.9 ± 0.7	KEK-E176 (1991) [53, 54]
$^{13}_{\Lambda\Lambda}$B	4.8 ± 0.7	KEK-E176 (1991) [53, 54]

Table 1.1: Presently available information on the effective binding energy $\Delta B_{\Lambda\Lambda}(^A_{\Lambda\Lambda}Z)$ between two Λ-particles. Note that $^{10}_{\Lambda\Lambda}$Be and $^{13}_{\Lambda\Lambda}$B correspond to the same event.

1.3.2 Towards electronic experiments detecting multi-hypernuclei

A drawback common to all theoretical investigations of double Λ-hypernuclei is the lack of high resolution and systematic data on multi-hypernuclei and their level structure. Although

analysis of emulsion stacks by automated means (e.g. by scanning the film with a CCD camera) has been found possible in some circumstances, these studies can not provide high production rates. Furthermore, if particle unstable states, whose decay photons are not detected, are populated or if neutrons are being emitted, this method gives ambiguous results.

The possibility to trigger via kaon detection on potentially interesting events clearly calls for experiments based on electronic detectors. Since the kinetic energies of the nuclear fragments are very low, these experiments have to rely on specific decay channels. In 2001 the AGS-E885/E906 collaboration published the first 'mass production' of about 30 $^{4}_{\Lambda\Lambda}$H events based on $\sim 10^{4}$ stopped Ξ^{-} [58]. The $\Lambda\Lambda$-hypernuclei are identified through the sequential weak decay via π^{-} emission which dominates in light nuclei. Since the pion kinetic energies are proportional to $\Delta B_{\Lambda\Lambda}$, coincidences between two pions help to trace the decay of the $\Lambda\Lambda$-nucleus. While this first spectrometer experiment could not determine the binding energies of $^{4}_{\Lambda\Lambda}$H (for alternative interpretations see [59]), the number of observed events is a signal that the production process of double hypernuclei is reasonable well understood.

2 Strangeness Nuclear Physics at the $\overline{\text{P}}$ANDA Experiment

The GSI facility will be upgraded in the next decade and a major component of the proposed international facility FAIR (see figure 2.1) will be the High Energy Storage Ring (HESR) for high intensity, phase space cooled anti-protons with momenta between 1.5 and 15 GeV/c. The $\overline{\text{P}}$ANDA experiment will be one of the key experiments at the Facility for Antiproton and Ion Research (FAIR) which is currently being built on the area of the GSI Helmholtzzentrum für Schwerionenforschung in Darmstadt (Germany). The $\overline{\text{P}}$ANDA collaboration was formed in 2002 and consists of about 400 physicists from 49 institutions in 16 countries. The detector is devoted to strong interaction precision studies in the transition energy range of perturbative QCD and non-perturbative QCD regime which exhibits large complexity but is essential for the understanding of nature [60]. Among the many experiments that are foreseen in $\overline{\text{P}}$ANDA (QCD bound states, electroweak physics, hadrons in nuclear matter, etc.), the one concerning this work is the hypernuclear physics research.

At the FAIR facility, anti-protons will be created by colliding high intensity protons with a copper target. These anti-protons will be collected, pre-cooled and finally stored in the High Energy Storage Ring (figure 2.2). The storage ring will deliver anti-proton beams of unprecedented precision ($\Delta p/p \approx 10^{-5}$) and intensity ($10^{11}$ circulating anti-protons in normal operation) that will hit an internal target [61].
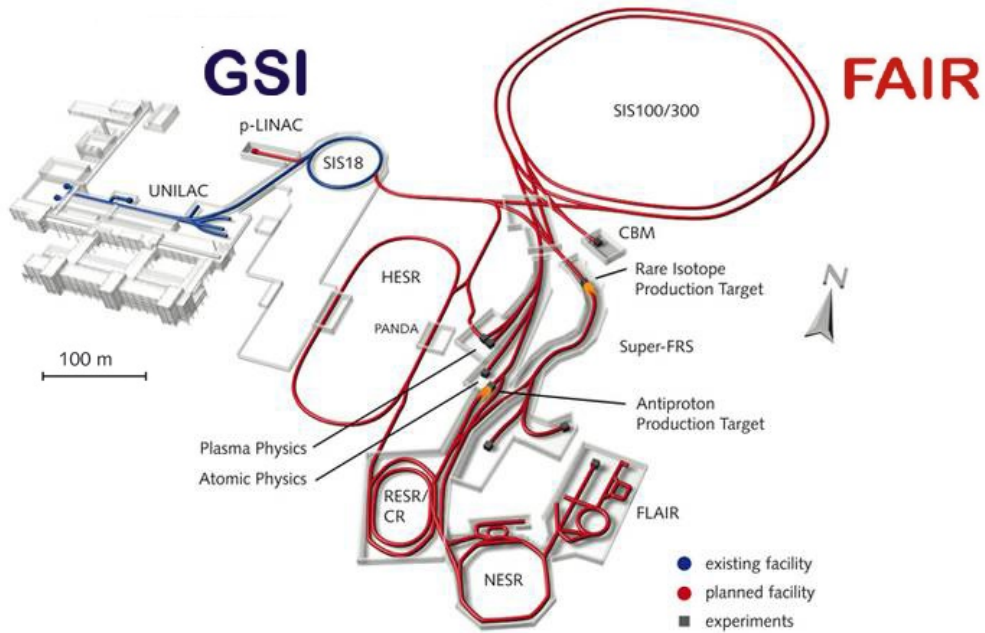
Figure 2.1: The FAIR complex at the GSI in Darmstadt.
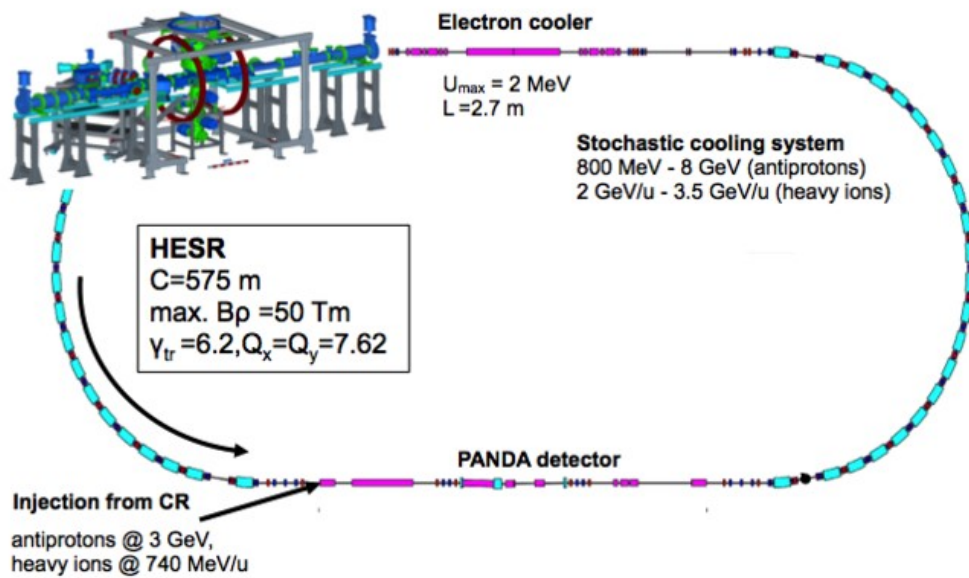
Figure 2.2: High Energy Storage Ring (HESR) at the FAIR facility.

The $\overline{\text{P}}$ANDA detector (figure 2.3) has to surround the target as completely as possible. To obtain a good momentum resolution the detector is subdivided into the target spectrometer (TS) consisting of a superconducting solenoid magnet surrounding the interaction region and measuring at high angles and a forward spectrometer (FS) based on a dipole to analyze the forward-going particles. The combination of two spectrometers allows a full angular coverage, it takes into account the wide range of energies and it still has sufficient flexibility, so that individual components can be exchanged or added for specific experiments, e.g. for the experiments with hypernuclei [62].
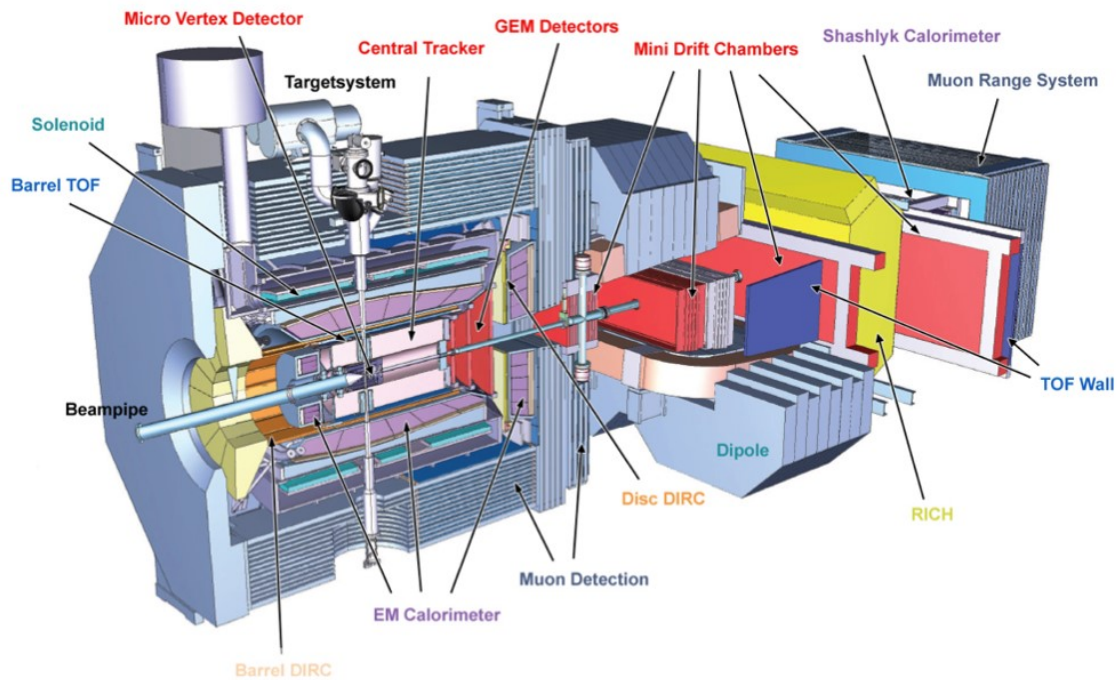
Figure 2.3: Artistic view of the $\overline{\text{P}}$ANDA detector [62].

Particles emitted with laboratory polar angles larger than 5° are measured in the target spectrometer. Surrounding the interaction volume there will be a silicon start detector followed by a silicon micro-vertex detector, 15 double-layers of crossed straw tubes and a cylindrical DIRC Cherenkov detector. The forward region will be covered by an aerogel Cherenkov detector using proximity focussing onto gas based photon detectors. These detectors are surrounded by an electromagnetic calorimeter consisting of $PbWO_4$ crystals. The target spectrometer is contained in a 2.5 m long and 80 cm radius solenoid. Behind the return yoke there will be ad-

ditional detectors for muon identification. Particles produced with polar angles below 10° in the horizontal and 5° in the vertical direction are measured with the help of a 1 m gap forward spectrometer dipole. Tracking detectors will be located before and behind the dipole. Particle identification will be obtained by a TOF-stop detector and a dual-radiator RICH detector. Behind this one there is a 3 m^2 lead glass calorimeter and a hadronic calorimeter followed by a muon detection system.

At $\overline{P}$ANDA, the production of hypernuclei and hyperatoms at HESR will use $\Xi\overline{\Xi}$ and $\Omega\overline{\Omega}$ pair production close to threshold in antiproton-nucleus collisions. The $\Lambda\Lambda$-hypernuclei will be created through a two-step process, as shown in figure 2.4. After the capture of the Ξ^-'s by a secondary nucleus, they are converted into two Λ-hyperons. The decays of the created double hypernuclei are then detected in the $\overline{P}$ANDA detector.
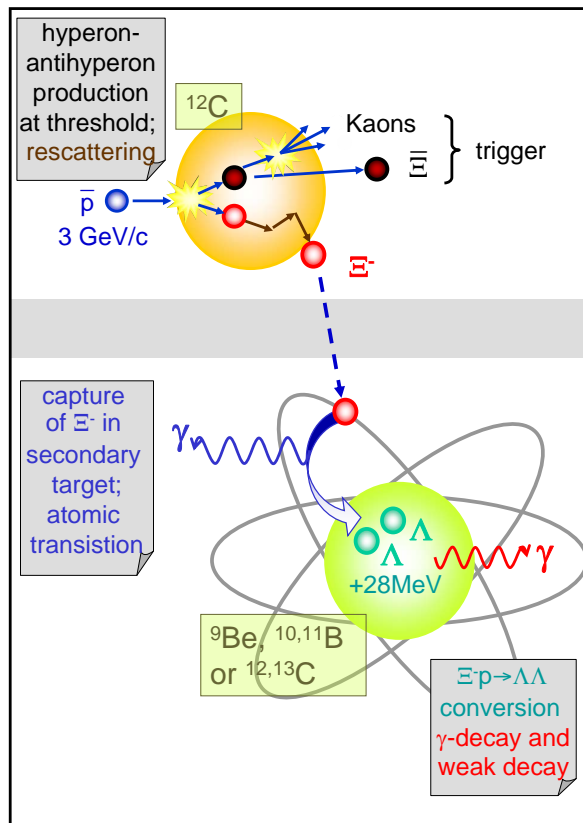
Figure 2.4: Schematic view of the formation steps of double hypernuclei at $\overline{P}$ANDA.

For the measurement of double-hypernuclei and hyperon-atoms the backward part of the calorimeter detector will be removed to place a dedicated primary target just before the straw tube tracker. Anti-protons at a momentum of 3 GeV/c will collide with a nuclear primary target (see figure 2.5) producing a pair of cascades via the reaction

$$\overline{p} + p \rightarrow \Xi^- + \overline{\Xi}^+ \tag{2.1}$$

The second ingredient of the experiment is the deceleration of the Ξ^- inside the nucleus and the subsequent absorption in an secondary active target. This secondary active target consists of a structure composed of silicon strip detectors with alternating layers of ^{9}Be, ^{10,11}B or ^{12,13}C absorber material (see figure 2.5) and is in charge of the slowing down, capture and conversion of the Ξ^- [dss] into two Λ [uds] via the strong interaction

$$\Xi^- + p \rightarrow \Lambda\Lambda + 28 MeV \tag{2.2}$$
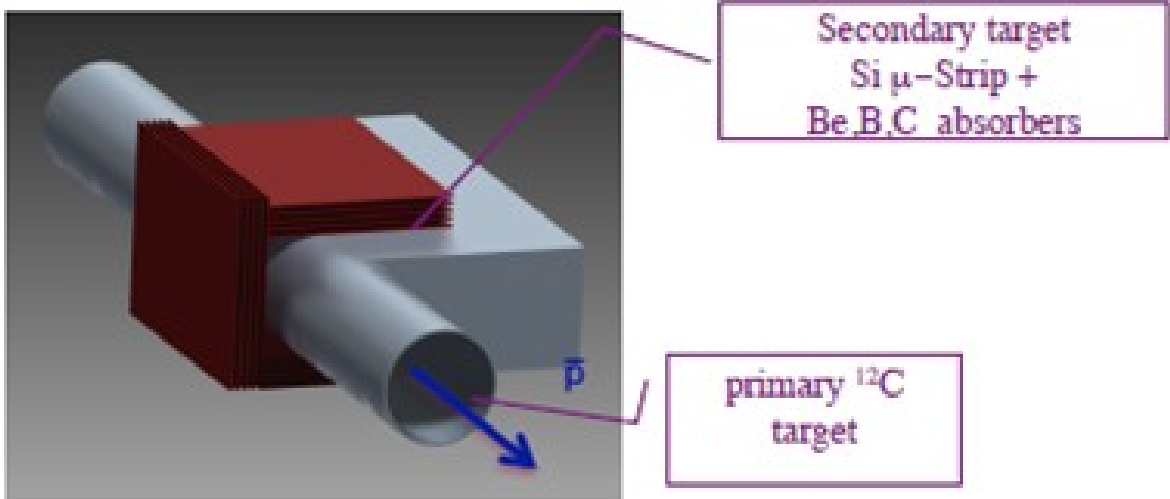
Figure 2.5: Schematic view of the primary and secondary target arrangement.

The geometry of this solid-state micro tracker is determined by the short mean life of the Ξ^- of only 0.164 ns. If the separation between the primary target and the secondary absorber is too large, low momentum Ξ^- will decay prior to full stopping. On the other hand, energetic Ξ^- with momenta beyond approximately 500 MeV/c can not be stopped prior to their decay. This limits the required thickness of the active secondary target to about a few 10 mm.

In order to track the stopped Ξ^- and the charged fragments resulting from the decay of the produced hypernuclei, it is planned to sandwich the absorber with solid state strip detectors. Spectroscopic information on double hypernuclei will only be obtained via their decay products, namely gamma-rays emitted from electromagnetic deexcitations and pions produced via the sequential mesonic decay. The γ-rays are detected by an array of 16 n-type germanium triple cluster-arrays which must be arranged as close as possible to the target. This array will be mounted at the backward angle outside of the superconducting solenoid magnet. Because of the expected high background rate due to hadronic reaction at the target, new fast readout electronics is presently being developed for the Ge detectors. In case of the hypernuclear spectroscopy the event selection will be based on the detection of two pions from the sequential weak decay of a light double hypernucleus. In figure 2.6 one can see how all the parts mentioned before are arranged inside the $\overline{\text{P}}$ANDA spectrometer.
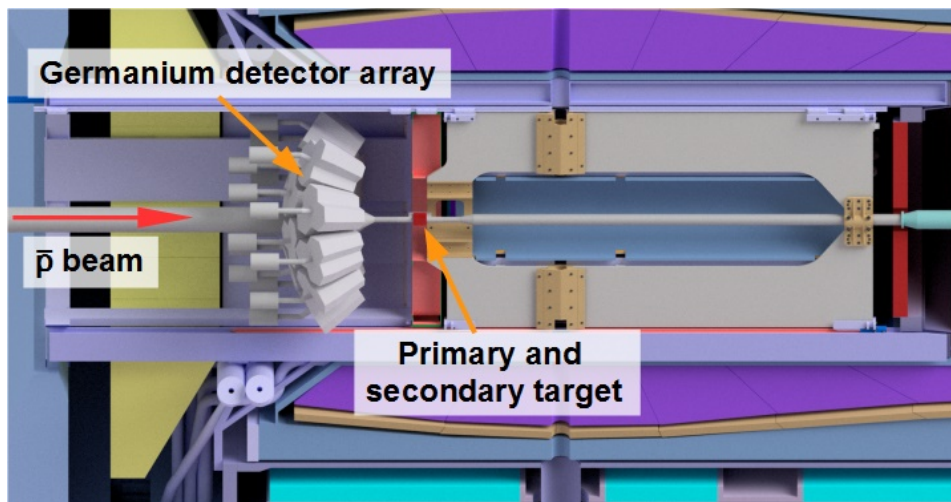
Figure 2.6: Setup for the production of hypernuclei inside the $\overline{\text{P}}$ANDA spectrometer.

My contribution to the $\overline{\text{P}}$ANDA experiment consists of the design and optimization of the primary target system for the production of $\Lambda\Lambda$-hypernuclei. In the next sections my work will be described, which comprises basically the three following tasks: selection of the primary target, design and test of a devoted target chamber and construction of a mechanism that permits to move and replace the primary target.

3 Primary Target

The Ξ^-'s will be produced by the reaction of the incident anti-protons in the primary target. In case of a complex nuclear target, these hyperons might rescatter inside that nucleus, thus lowering their momentum prior to their emission. In a second step, the Ξ^-'s may eventually be stopped and absorbed in a secondary target (see figure 2.4). In the following section, the arguments that need to be considered in selecting the target material will be exposed. Taking all different arguments into account, it turns out that a carbon target will provide a high stopping rate for Ξ^--hyperons at $\overline{P}ANDA$ as well as low anti-proton losses in the HESR. In the subsequent section 3.2, the first target prototype which consists of a diamond filament will be described as well as the radiation test performed on it at the MAMI accelerator.

3.1 Requirements of the primary target

The selection of the target nucleus obviously affects the production rate of Ξ^-'s. In addition, the amount of hadronic background, e.g. neutrons, will depend on the choice of the target too. Furthermore, the geometry and stability issues have to be considered for the operation in a storage ring.

Ξ^- **production:** The Ξ^--hyperon production rate must be as high as possible to achieve a copious generation of double hypernuclei. Moreover, in order to reach a high capture probability of the Ξ^- in the secondary target, it is mandatory to keep the primary momentum of the produced Ξ^- as low as possible. Ξ^--hyperons with momenta above 500 MeV/c have a stopping time which exceeds their lifetime and hence the Ξ^- would decay prior to the atomic capture with high probability.

18

In reference [63] a simplified cascade model was used to simulate the $\overline{p} + A \rightarrow \Xi + \overline{\Xi}$ reaction. In these simulations the beam pipe and secondary target were assumed to be simply a hollow tube surrounded by absorber material. Six different nuclei ranging from light (^{12}C) to heavy (^{197}Au) were considered in order to work out the efficiency of Ξ^- production and slowing down inside the nucleus as a function of the mass number A. For that study, the target shape has been chosen as simple as possible, a wire of 10 μm diameter. The results of the estimated number of Ξ^-'s absorbed in the production nucleus, decayed somewhere in flight within the two-target setup or brought to rest in the secondary target for the simulated targets are summarized in table 3.1. The numbers show the percentage of absorption, decay in flight and stopping defined as the ratio between the previously mentioned magnitudes and the total number of generated Ξ^-'s [63].

Material	Absorbed ($\pm 0.06\%$)	Decayed ($\pm 0.06\%$)	Stopped ($\pm 0.004\%$)
^{12}C	19.46	80.33	0.213
^{27}Al	24.47	75.26	0.268
^{59}Ni	30.11	69.56	0.325
^{108}Ag	35.25	64.40	0.352
^{137}Ba	37.41	62.23	0.360
^{197}Au	40.70	58.91	0.391

Table 3.1: Percentage of Ξ^--hyperons absorbed in the primary target nucleus, decaying in flight or stopped in the secondary target for different materials of the primary target (from reference [63]).

In the meantime more precise calculations were carried out on ^{12}C, ^{28}Si and ^{48}Ti with events generated by the GiBUU code [64] and taking the detailed geometry of the hypernucleus setup into account [65]. Similar to the schematic simulations of reference [63], these more reliable simulations also predict an increase of the rate of stopped Ξ^-'s for targets heavier than ^{12}C (see second column in table 3.2). However, as will be discussed in the following paragraph, with increasing mass and charge number of the target the losses of anti-protons increase as

well.

Material	Ξ^- **production rate**	Ξ^- **stopping rate** [%]	σ_h/σ_{total}	FoM
^{12}C	$2.21 \cdot 10^{-5}$	0.544	0.539	$6.47 \cdot 10^{-8}$
^{28}Si	$3.75 \cdot 10^{-5}$	0.724	0.339	$9.20 \cdot 10^{-8}$
^{48}Ti	$5.15 \cdot 10^{-5}$	0.626	0.245	$7.89 \cdot 10^{-8}$

Table 3.2: Ξ^- production rate, percentage of hyperons stopped in the secondary target for different primary target materials as predicted by GiBUU and full GEANT simulations and fraction of anti-protons inducing a hadronic interaction. The last column shows the product of these three numbers as a figure-of-merit [65].

Reduced luminosity due to beam losses: Any losses of anti-protons should be minimized to reach high luminosities. That means that the particle losses, mainly due to Coulomb scattering, should be kept low because the anti-proton production rate is limited. Coulomb scattering and energy straggling in heavy targets leads to significant losses of anti-protons. The beam loss rates due to the hadronic interaction, single Coulomb scattering, energy straggling and Touschek effect have been calculated for each solid target mentioned before [63]. In particular, the Touschek effect rates have been found to be negligible in comparison with the hadronic, single Coulomb interaction and energy straggling [66, 65]. The fourth column in table 3.2 gives the fraction of anti-protons in the HESR that can contribute to hadronic interactions (which eventually lead to Ξ^- production). For the calculations the formulas given in reference [66] were used. Combining the Ξ^- production rate with information on the beam losses, the schematic calculations of reference [63] clearly preferred ^{12}C as a primary target. In the more detailed calculations based on GiBUU events and on full GEANT simulations, the situation is less clear. The last column in table 3.2 shows as a figure-of-merit (FoM) the product of the Ξ^- production rate, the stopped Ξ^- rate and the fraction of anti-protons available for hadronic interactions. The FoM even slightly increases when going from ^{12}C to ^{28}Si. Consistent with reference [63] it then decreases substantially for heavier primary targets. As will be shown in the next paragraph, there are, nevertheless, further arguments in favor of the

lightest possible target material.

Hadronic background: The hadronic background should be minimal in the backward direction where the Germanium detectors are located, otherwise they would be damaged. For lighter targets the particles are preferentially focused in the forward direction, thus reducing significantly the number of particle hits in the germanium detectors. Moreover, because of the larger neutron-to-proton ratio in heavier targets, lighter target nuclei reduce the neutron background. Also the x-ray background is lower energetic for light nuclei and does not affect the γ-spectra. In addition, the silicon detectors of the secondary target which cover laboratory angles beyond 45° are less loaded by more forward emitted particles in case of light targets [65].

Thermal conductivity and geometry: The thermal conductivity of a material describes its capacity to conduct heat. Heat transfer occurs at a lower rate across materials of low thermal conductivity than across materials of high thermal conductivity. When a target is irradiated with a beam of particles with high energy, its temperature rises enormously. For the experiment a target with a high coefficient of thermal conductivity is needed so that it can diffuse the heat, otherwise it would not resist such high temperatures and would be burned by the anti-protons. Furthermore, a target with reduced size and thickness of typically a few $10\,\mu$m is required to keep the interaction rate at the required level of few times 10^6. The thickness of the primary target is also constrained by small angular scattering causing beam heating (see above). It must be pointed out that the thickness of the primary target is not critic as far as the hyperon slowing down is concerned, since the ionization energy loss is completely negligible over distances of the order of micrometers.

Conclusion: Taking all these arguments together, the choice of a light nucleus as a primary target material is favored. Luckily, with diamond or carbon micro-fibers one has a material at hand which has exceptional mechanical, electrical and thermal properties as will be shown in the next section. It is clear, though, that the survival of such a target in an internal target experiment like $\overline{\text{P}}$ANDA with high beam interaction rates is a critical issue and needs confirmation.

Silicon and titanium are also considered as possible target materials. In the next section, the properties of the possible target materials will be commented. Furthermore, a description of the diamond target prototype and of the radiation test performed on it at the MAMI accelerator will be given.

3.2 Prototypes for the primary target

According to the results of the simulations presented in the previous section the most appropriate material for the primary target is ^{12}C although other elements like ^{28}Si and ^{48}Ti have been conceived too. Two targets made of carbon have been considered: a diamond filament and a carbon microfiber. The first one has already been produced and tested. Diamond has been chosen because of its high thermal conductivity and stiffness. The selected shape of the first target prototype is a diamond micro-wire with a width of 100 μm that is cut out of a 3 μm thick CVD diamond disc by LASER cutting. The filament is held in a circular silicon frame with an outer diameter of 15 mm as in figure 3.1. The properties of the target and its support frame are listed in table 3.3.

Target	material	CVD diamond
	density	3.52 g/cm^3
	thickness	3 μm
	width	100 μm
	areal density	$1.056 \cdot 10^{-3}$ g/cm^2
Support frame	material	silicon
	density	2,33 g/cm^3
	thickness	500 μm
	outer diameter	15 mm
	inner diameter	11 mm

Table 3.3: Properties of the diamond primary target prototype and its support frame [65].
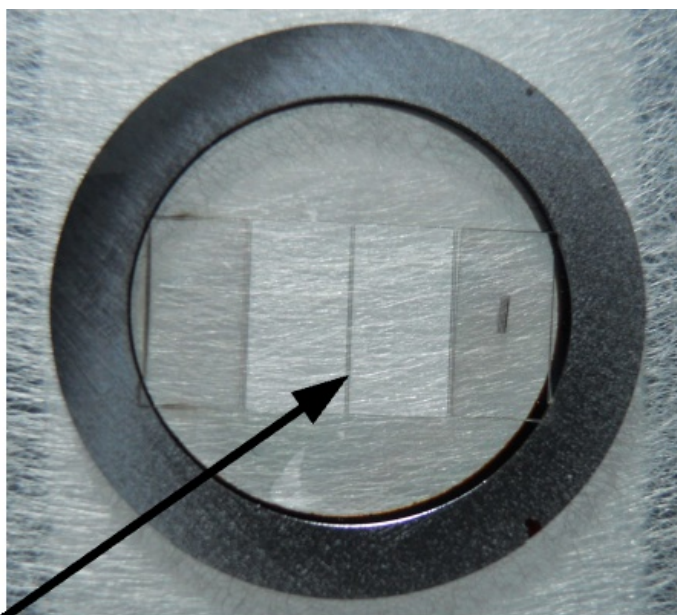
Diamond micro-wire

Figure 3.1: Primary target: diamond micro-wire with 3 μm thickness and 100 μm width held in a circular silicon frame with an outer diameter of 15 mm [67].

For a second target prototype the use of pitch based carbon fibers DIALEAD produced by Mitsubishi Rayon has been considered. Microfibers allow to have targets with diameter in the range of only a few micrometers. DIALEAD has a high carbon content ratio, maintaining chemical stability of composite materials. It has a structure in which graphite plates are highly oriented in the vertical direction of the fiber. This results in such features as lightweight, high stiffness, high thermal conductivity and an ultra low thermal expansion coefficient [68]. Specifically, among the available DIALEAD fibers, the continuous fiber K13D2U has been selected because it has the highest thermal conductivity. Each fiber contains approximately 10000 filaments, the target will be built of a single extracted filament. Since the delivery and thus the production of a target made of such a fiber was delayed, this target material could not be studied within this thesis but it is planned to prepare and test such a target in the near future [65].

In table 3.4 the properties of the considered possible target materials (diamond, carbon fibers,

silicon and titanium) are compared with the ones of copper, which is the material typically selected for applications where high temperatures might occur. Copper has very good electrical and thermal properties, however, table 3.4 demonstrates the superior features of diamond and carbon fibers as they have significantly higher thermal conductivity and tensile modulus.

Material	Thermal conductivity (W/mK)	Tensile modulus (°C)	Density (g/cm^3)
Diamond [69]	1800-2500	1050-1210	3.52
DIALEAD K13D2U [68]	800	935	2.20
Silicon [70]	149	130-185	2.33
Titanium [71]	22	110	4.51
Copper [72]	401	120	8.96

Table 3.4: Properties of possible primary target materials compared with copper as a reference.

3.2.1 Target radiation test at MAMI

A radiation test has been carried out at the MAMI facility to see if the diamond filament breaks or suffers damages due to the thermal stress. The Mainz Microtron (MAMI) is an accelerator for electron beams run by the Institute for Nuclear Physics of the University of Mainz that is used for hadron physics experiments. It is set up as a multilevel racetrack microtron with a normal conducting linear accelerator. It supplies an electron beam with a maximum energy of 1508 MeV and a maximum current of 100 μA. The accelerator has a length of 8.9 m and operates in a magnetic field of 1.28 T [73].

The radiation test has been performed from the night of 21.10.2015 to the morning of 22.10.2015. The diamond micro-wire has been placed in a vacuum chamber with a pressure of 10^{-7} mbar and has been irradiated by an 855 MeV electron beam with an intensity of 0.5 μA during approximately 9 hours. Figure 3.2 shows the schematic view of the experimental setup seen from above. The electrons enter the vacuum chamber from the left and hit the diamond target that is placed inside. The magnet located behind the vacuum chamber deflects the electrons into

the beam dump. For the correct positioning of the target in the beam and the determination of its width, the ionization chamber is important: the more interactions with the target take place the more electrons are slightly shifted from the unaffected path and enter the ionization chamber. The given voltage is then a direct measure of the interaction rate. A look to the interior of the chamber where the target is located is shown in figure 3.3 where the electron beam comes from the bottom and hits the diamond filament that is held in a frame like the one of the zoomed image.
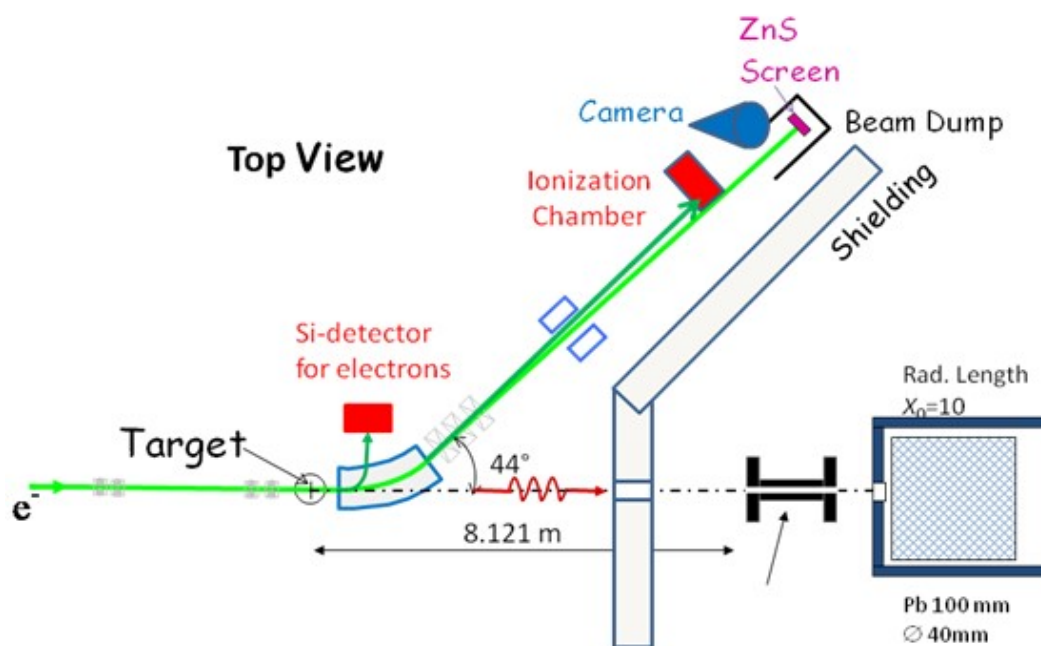
Figure 3.2: Schematic view from above of the experimental setup used for the irradiation of the diamond micro-wire at the MAMI facility.
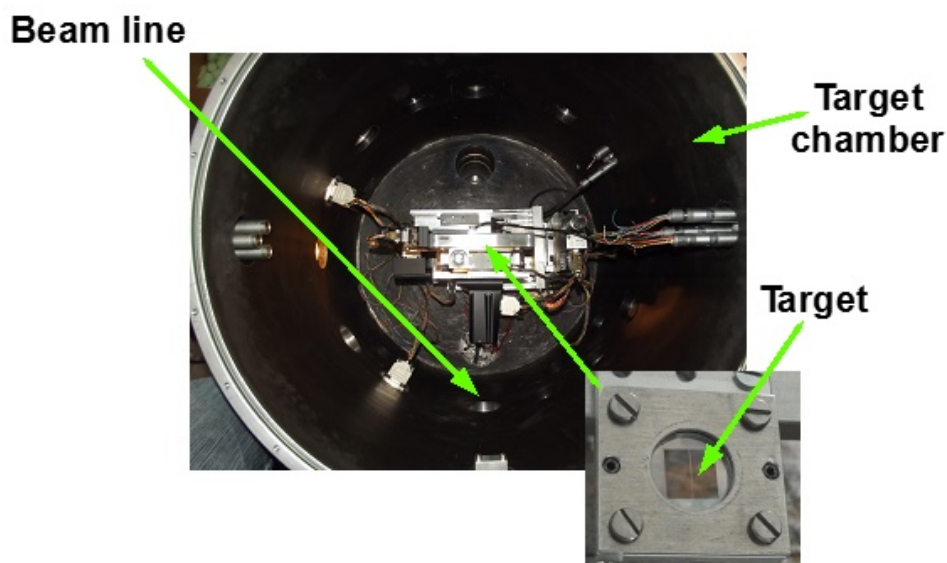
Figure 3.3: Closer look to the interior of the vacuum target chamber.

The electron beam has a two-dimensional gaussian profile. In the beam preparation process it has been intended to get a minimal full width at half maximum (FWHM) value -in the order of $100\,\mu$m- so that the majority of the electrons cover the target. After the beam steering the target has been centered by means of an ionization measurement. To determine the actual beam width an ionization scan has been performed in which the target passes through the beam. This scan is needed since the beam width has similar size as the diamond filament and determines the number of electrons passing through it. However, the beam width is not exactly known. Scanning the beam with constant velocity and the diamond filament with known thickness, one can determine the diameter of the beam. The measured voltage against the time shows a gaussian distribution that is a convolution of a rectangular function (target) with the gaussian beam profile. With the speed of the target ($10\,\mu$m/s) the time axis can be transferred into a unit of length. For the folded distribution a FWHM of $195.3\,\mu$m has been determined. Figure 3.4 illustrates the obtained FWHM values in a numerical convolution of a normal distribution with different widths and a fixed rectangular function that represents the target shape. Metering the graph at $195.3\,\mu$m on the ordinate leads to a FWHM of the beam of $182.5\,\mu$m. The fitted graph of the ionization scan as well as the deduced results are visualized in figure 3.5.

Convolution of gaussian beam profiles with fixed rectangular target
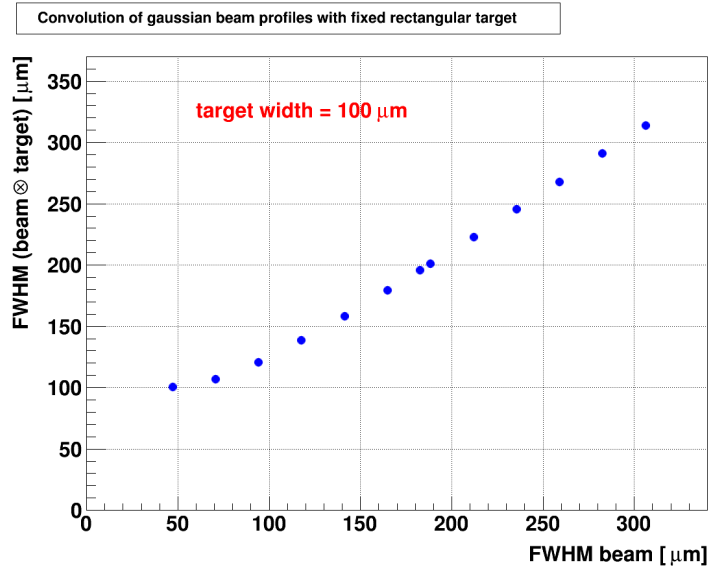
target width = 100 μm

Figure 3.4: Gaussian beam profiles folded with the target width [65]. In reverse metering it is possible to identify the beam width that belongs to a measured FWHM of 195.3 μm.

Deconvolution of the ionisation measurement

χ^2 / ndf	0.4585 / 2726
offset [V]	0.0527 $\pm$ 0.0004399
A [V]	1.701 $\pm$ 0.0007058
μ [μm]	675 $\pm$ 0.03602
σ [μm]	82.92 $\pm$ 0.04737

- ionisation measurement
- convolution
- beam profile (σ_x = 77.5 μm)
- target (width = 100 μm)
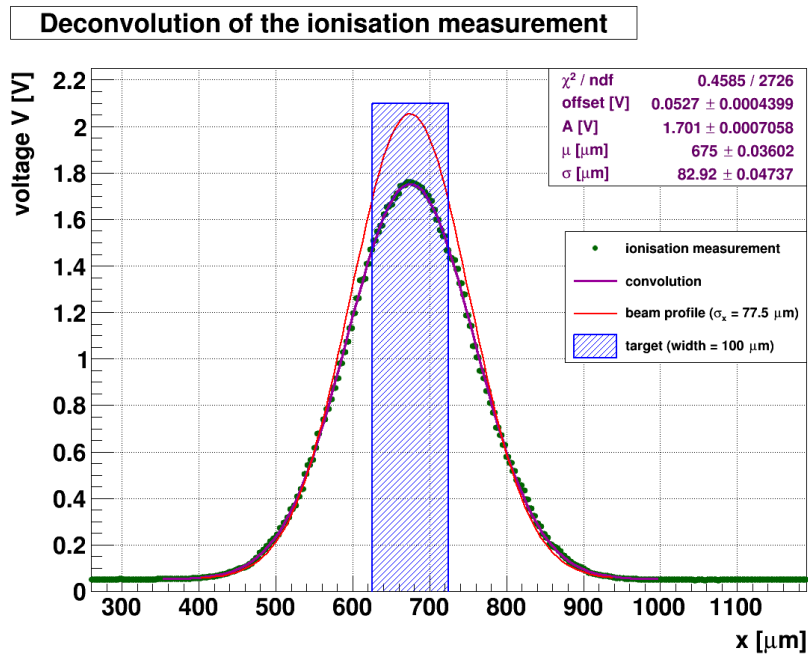
Figure 3.5: Picture of the situation during the beam test [65]. The target (blue) is centered with respect to the beam (red). The width of the beam profile is derived from the deconvolution of the ionization measurement (green points).

27

The electron beam centered on the target corresponds to an overlap of f = 48.1%, which means that this fraction f of the beam is hitting the target. The number of electrons on the target per second R_e is:

$$R_e = f \cdot \frac{I_{beam}}{Q_e} = 1.5 \cdot 10^{12} \ e^-/s \tag{3.1}$$

The stopping power of electrons in collisions with carbon at E_{kin} = 849.5 MeV is 2.1 MeV·cm^2/g [74]. The energy loss ΔE_e of electrons in collisions is then given by the product of the stopping power and the areal density of diamond, which is ΔE_e = 2.2 keV [75]. This leads to a power of 0.53 mW calculated by the energy loss per electron passing the target times the number of electrons per second on the target.

During the whole beam time the measured ionization rate stayed constant for several hours. Hence, the most important finding has been that the filament does not break under these conditions what means that the heat transport of the diamond is sufficient to diffuse the deposited energy. Nevertheless, as a consequence of the irradiation a small black spot in the middle of the diamond micro-wire appeared. As a first step, the target has been observed with a microscope obtaining the image of figure 3.6. A more detailed analysis by using Raman spectroscopy is foreseen to clarify if the black spot has been originated due to a change in the inner structure of diamond or if residual gases in the vacuum chamber have burned up the filament.

The energy deposition of the electrons on the target at MAMI has to be calculated to see if it is comparable to the energy deposition of the anti-protons at $\overline{P}$ANDA and thus if the diamond filament would survive under its operating conditions. The power dissipation at $\overline{P}$ANDA with anti-protons instead of electrons and with a beam FWHM in the order of 1 mm will be 0.056 mW [65], thus a factor about 10 lower than at MAMI. Therefore, the performed beam test shows that the experimental conditions at $\overline{P}$ANDA are not critical concerning thermal stress on the diamond micro-wire.

In the near future, the carbon fibers will also be investigated in irradiation tests. With a heat conductivity of 800 W/mK, the fibers are worse diffusing heat than diamond by a factor of

Figure 3.6: Black spot on the diamond filament after being irradiated with electrons.

about 2.7. Furthermore, considering the fact that the electron beam at MAMI has a significant smaller size ($\sim$0.2 mm) as compared to the expected anti-proton beam at $\overline{P}$ANDA (1 mm), no thermal damage is expected to occur for the filament target. Currently, silicon can not be ruled out yet since further investigations to test its feasibility as target material must be carried out. Moreover, it has been proven that elements heavier than silicon are not suitable for the experiment.

4 Target Chamber

Once that the material and the shape of the primary target have been studied, it is important to design a devoted chamber that fulfills the physical and technical requirements of the $\overline{\text{P}}$ANDA experiment. In the following sections, the designs and mechanical tests of the target chamber will be presented.

4.1 Target chamber designs

For the design of the chamber in which the primary target will be placed some requirements must be taken into account. The first one is that, although it would be recommendable to minimize the distance between the primary and secondary targets to reach a high Ξ^- stopping rate, this distance is limited by the inner diameter of the anti-proton beam pipe of $\overline{\text{P}}$ANDA, which is 20 mm. For that reason, the internal height of the chamber can not be below 20 mm. The second requirement is that the Ξ^-'s produced in the primary target have to be able to go through the chamber walls and reach the absorbers. That is why it has been thought of using a thin window material surrounding the primary interaction point. One can see a CAD drawing of this model of target chamber with its corresponding dimensions in the left part of figure 4.1. The part of the chamber colored in orange is the window material. Another point to consider is the mechanical stability of the chamber so that the walls do not bend significantly to the inside when high vacuum is applied. Different foils have been glued on two target chamber frames, one with rectangular edge and another one with rounded edge, like the ones on the right part of figure 4.1. The reason of using two different frames is to see whether the shape of the edges influences the bending of the window foils when the chamber is pumped.
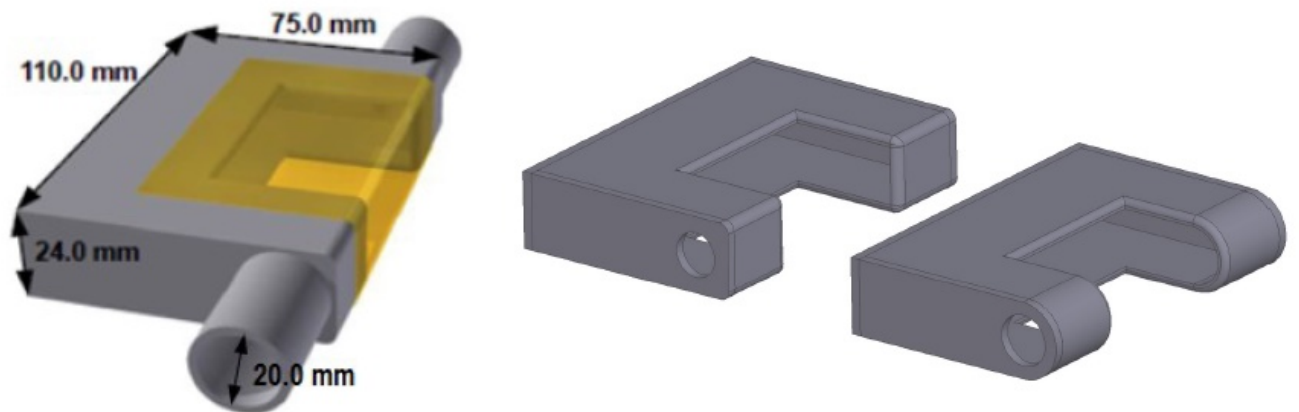
Figure 4.1: Left side: CAD drawing with dimensions of the target chamber model with the window material colored in orange surrounding the primary interaction point [76]. Right side: CAD drawings of the chamber frames with rectangular and rounded edges.

The bending to the inside of the window foil when the chamber is pumped should be minimized since 20 mm free space is needed in the interior of the chamber for the beam pipe. Furthermore, the foils should resist several pumping cycles without breaking and without increasing the deformation. Therefore, the mechanical stability of this chamber model has been studied for different window foils, as will be described in the next section.

4.2 Deformation of the window materials

The window material for the target chamber has to accomplish basically three requirements. The first one is that the material budget has to be kept low so that as many Ξ^- as possible can go through it and reach the absorbers behind. The second one is that the material should not bend too much to the interior of the chamber when vacuum is generated because that would interfere with the anti-proton beam what implies that the inner height of the chamber should be increased thus having the secondary absorbers further from the primary target, what is not

convenient for a high Ξ^- stopping and absorption rate. A maximum bending of 1 mm would be advisable. The last requirement is that the material should remain stable in time, what means that after many cycles of evacuation and decompression the deformation of the window should not vary significantly and the material should not break or tear.

Some materials have been selected as candidates for the target chamber window according to their densities. Foils of these materials with variable thicknesses have been glued on the two chamber frames of figure 4.1. The following foils have been tested on the rectangular frame: Kapton 140 μm, Upilex-s 125 μm, Brass (CuZn) 200 μm, Ti 200 μm and AlMg 250 μm. And these ones on the rounded frame: Brass (CuZn) 200 μm, Ti 140 μm, Ti 200 μm, AlMg 100 μm and AlMg 200 μm. The ten chambers that have been tested are shown in figure 4.2.

Figure 4.2: All the target chambers that have been tested.

In the next two sections, the procedure to measure the bending of the window materials as

well as the results of the maximum deformation of the foils after one pumping cycle and after several cycles will be commented.

4.2.1 Deformation after one cycle

To measure the bending of the foils a grid like the one of the right side of figure 4.3 has been drawn on the area of the material window with a separation of 5 millimeter between each point. All the chambers have been evacuated up to a pressure of 10^{-5} mbar by connecting them to a vacuum pump. The deformation has been measured on each point of the grid and for both sides of the chamber with the help of a precision needle (left side of figure 4.3). One can see that some of the chambers are strongly bent to the inside when being pumped, like the one made of AlMg of 100 μm thickness and rounded shape on the right side of figure 4.3.

Figure 4.3: Left side: Chamber connected to the vacuum pump with the precision needle measuring its deformation. Right side: AlMg 100 μm rounded chamber deeply deformed when pumped.

The deformation of each point of the grid has been plotted for each of the chambers. The plot of the bending of one of the faces for the AlMg 100 μm rounded shape chamber is shown in

figure 4.4 as example, according to the reference system drawn in figure 4.3, where x ∈ [0, 3] cm and y ∈ [0, 6] cm. One can observe clearly in the figure that the deformation in the center of the window is very strong, with a depth of 2.2 mm at the maximum deformation point.
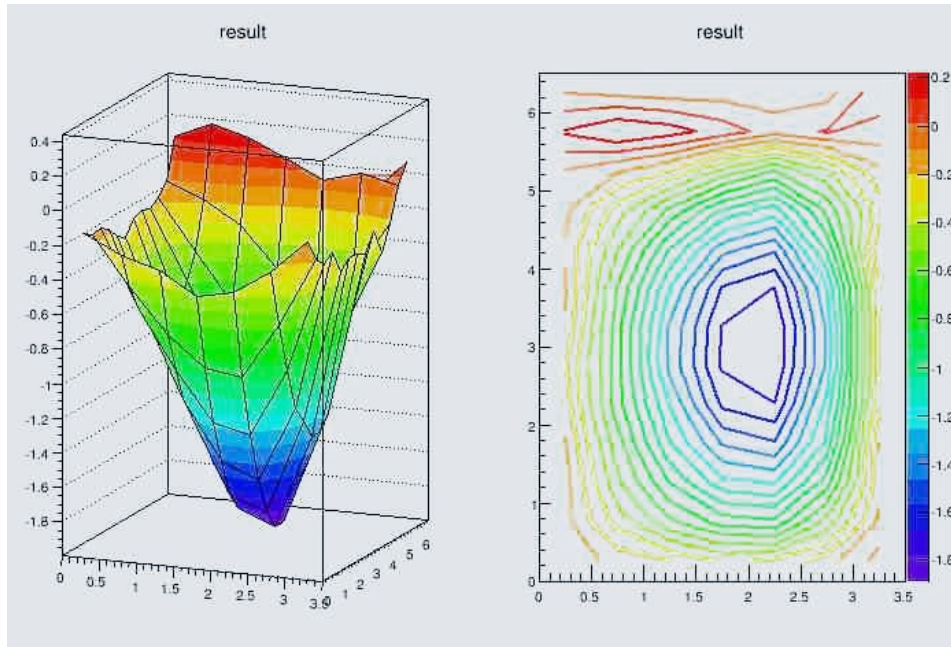
Figure 4.4: Plot of the deformation of the AlMg 100 μm rounded shape chamber.

After measuring the deformation for all the points of the grid, the maximum deformation point has been searched for each of the chambers by displacing the needle over the surface of the window material. The results of the maximum bending points of the foils are collected in table 4.1. Although the accuracy of the apparatus is 0.001 mm, it has been considered an error of 0.01 mm due to the big manual error. The maximum deformation points are plotted for each of the chambers in figure 4.5. In the plot one can analyze the dependence of the bending with the areal density of the material. As expected, the deformation of the window decreases with increasing areal density of the foil. But even for rather thick foils the deformation exceeds 1 mm. Concerning the shape of the edge of the chamber, there is no clear trend visible. While for the 200 μm Ti foil the deformation for both edges is almost the same, for the brass foil the rectangular shape bends less than the rounded one. The plot shows that the Kapton and UPILEX-S foils can be discarded due to their significant bending. From the study one can

also deduce that in every case the deformation of the bottom and top faces of the chamber is practically the same.

Material	Density (g/cm^3)	Shape	Thickness (μm)	Maximum depth ($\pm 0.01mm$)
Titanium	4.54	Rounded	200	1.22
Titanium	4.54	Rounded	140	2.08
Titanium	4.54	Rectangular	200	1.17
AlMg	2.66	Rounded	200	1.86
AlMg	2.66	Rounded	100	2.20
AlMg	2.66	Rectangular	250	1.33
Brass	8.50	Rounded	200	1.42
Brass	8.50	Rectangular	200	1.12
UPILEX-S	1.47	Rectangular	125	3.70
Kapton	1.42	Rectangular	140	4.72

Table 4.1: Maximum bending points of the different foils.
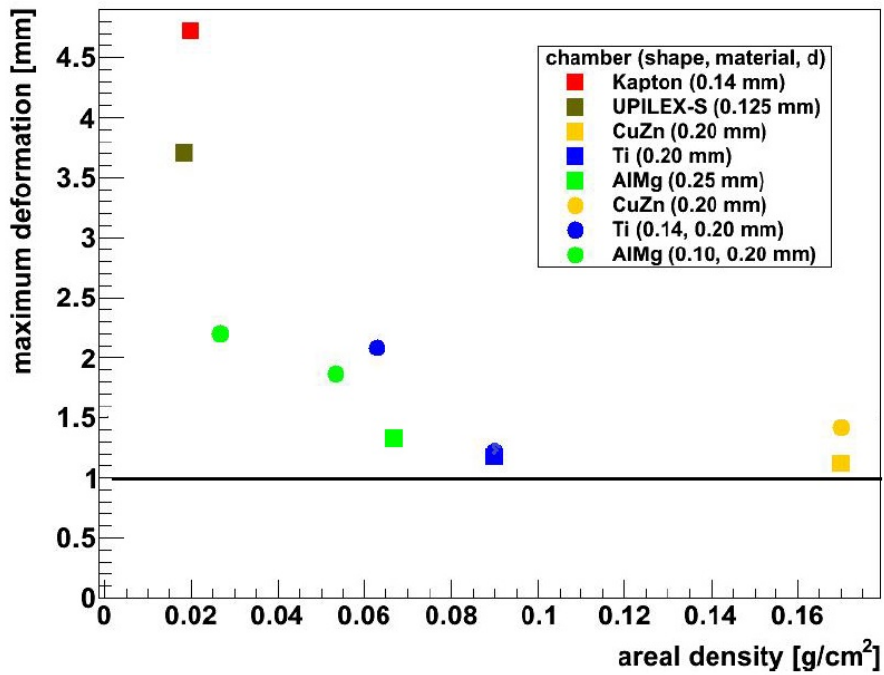
Figure 4.5: Maximum deformation as a function of the areal density of the window materials. Squared symbols correspond to chambers with rectangular edge and circular symbols to chambers with rounded edge.

4.2.2 Deformation after many cycles

This time each of the chambers has been evacuated several times to see if the deformation of the foils depend on the number of pumping cycles. Every 100 cycles the maximum deformation point has been measured by using the method of the previous section. For most of the chambers the dependence of the bending with the number of cycles is negligible, however, some of them get appreciably more deformed. The AlMg chamber with a thickness of 250 μm and rectangular shape even tore at one edge after 1560 cycles, as one can see in figure 4.6. For this chamber, the dependence of the maximum deformation on the number of cycles has been plotted in figure 4.7 from the cycle 1000 that is when the bending starts to vary with the number of cycles and up to the cycle 1560 that the foil tears. One can observe that the deformation of the left side of the chamber (blue points) increases more with the number of cycles as the right side (red points), which remains more or less constant.
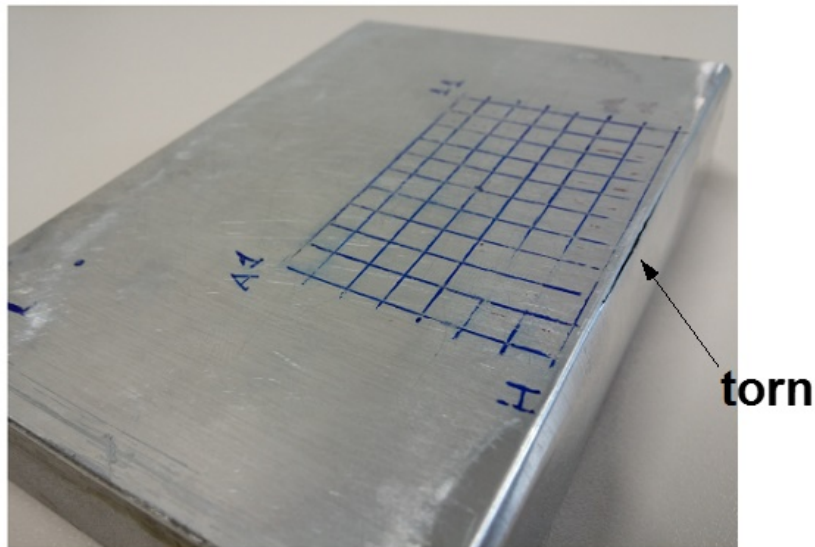
Figure 4.6: AlMg 250 μm rectangular shape chamber torn at one edge after many vacuum cycles.
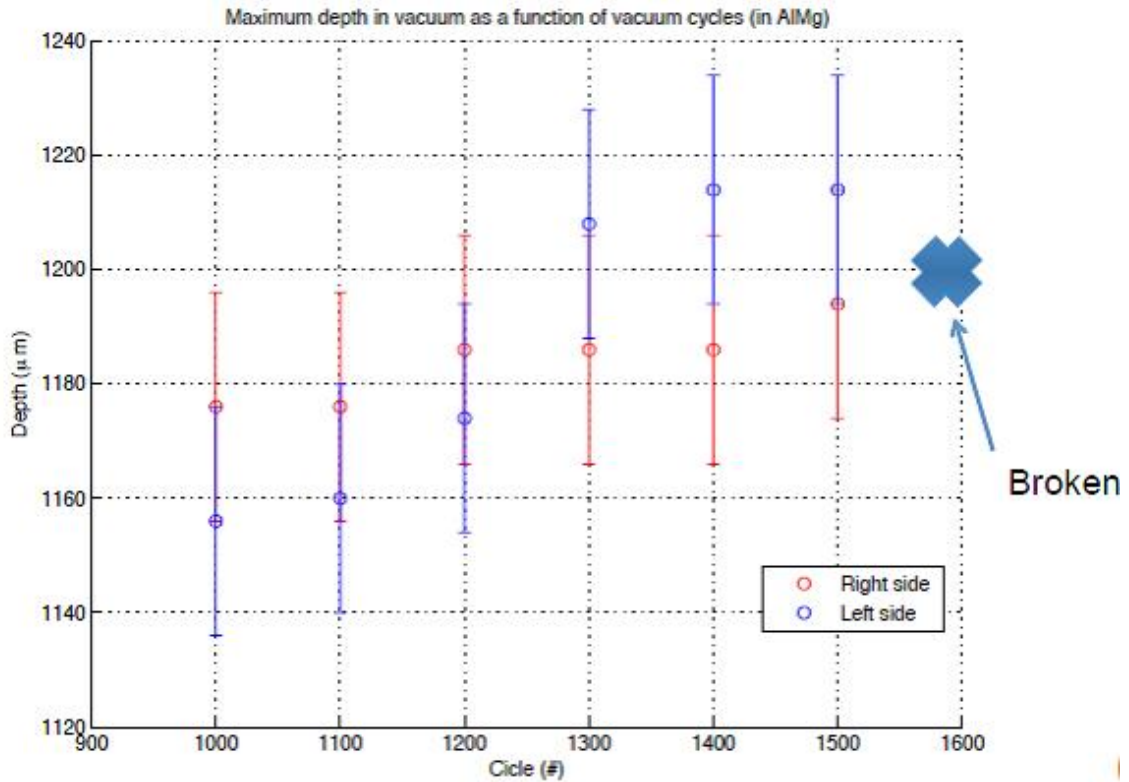
Figure 4.7: Maximum deformation of both faces of the AlMg 250 μm rectangular chamber as a function of the number of cycles of evacuation and decompression. Material torn after 1560 cycles [77].

For all the foils, the deformation begins to increase only after many pumping cycles ($\sim$1000). This is not relevant for the operation of $\overline{P}$ANDA since we expect only a few pumping cycles. The study of the deformation of the chambers shows that the idea of separating the secondary target from the target chamber, although it is a possible solution, has some disadvantages. The mechanical stability of the materials is not fully reliable and the deformation to the inside of all the selected foils is bigger than 1 mm which would be the advisable limit since 20 mm free space is needed inside the chamber for the beam pipe. To keep the free 20 mm inside the chamber counting the bending, the distance between the primary target and the secondary target absorbers should then be increased what is not favorable for the maximum absorption of the Ξ^-'s. Moreover, the use of the foil causes some losses of Ξ^-'s that decay before they can pass through it. That is why it would be preferable to put the absorbers directly integrated

in the chamber. A new model has been designed where a carbide of the absorber material is placed surrounding the primary target and its corresponding absorber directly on it. In figure 4.8 one finds on the right side the CAD drawing of the new chamber frame and on the left side the prototype that has been already built. This chamber has been pumped observing that no deformation of the absorber window is produced.
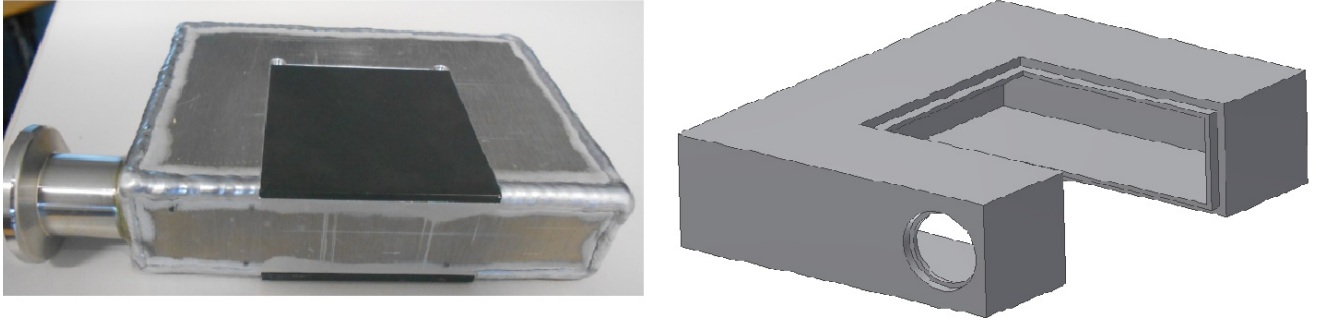
Figure 4.8: Left side: new target chamber prototype. Right side: CAD design of the frame of the new chamber model.

In the next chapter, the design of a devoted system that permits to move and replace the primary target will be presented. The tests performed on the piezo-motor that carries the target and the procedure followed to arrange all the components together and run the system will be described as well.

5 Moving system of the primary target

For the experiment a movable target is needed so that it can be removed during beam preparation time and to keep the luminosity of the beam constant. It can be that the target suffers damages after being irradiated by the anti-proton beam so a system that permits an easy replacement of the target is required. For that purpose, a system like the one of figure 5.1 has been designed and built. In this setup five piezo-motors are arranged in parallel, each one carrying a target, so that if the target that is being irradiated breaks, it can be replaced with the help of the next motor in the right position (center of the beam line). The motors are located on a movable stage that can be displaced by the HR1-U motor of figure 5.1. An encoder enables to know the position of the target with respect to the beam by reading the position of the stage through a glass scale. All the components of the setup are very small and suitable for working in ultra-high vacuum and in a magnetic field of up to 2 T. In figure 5.2, one can see the primary target system together with the secondary target incorporated in the $\overline{\text{P}}$ANDA spectrometer.
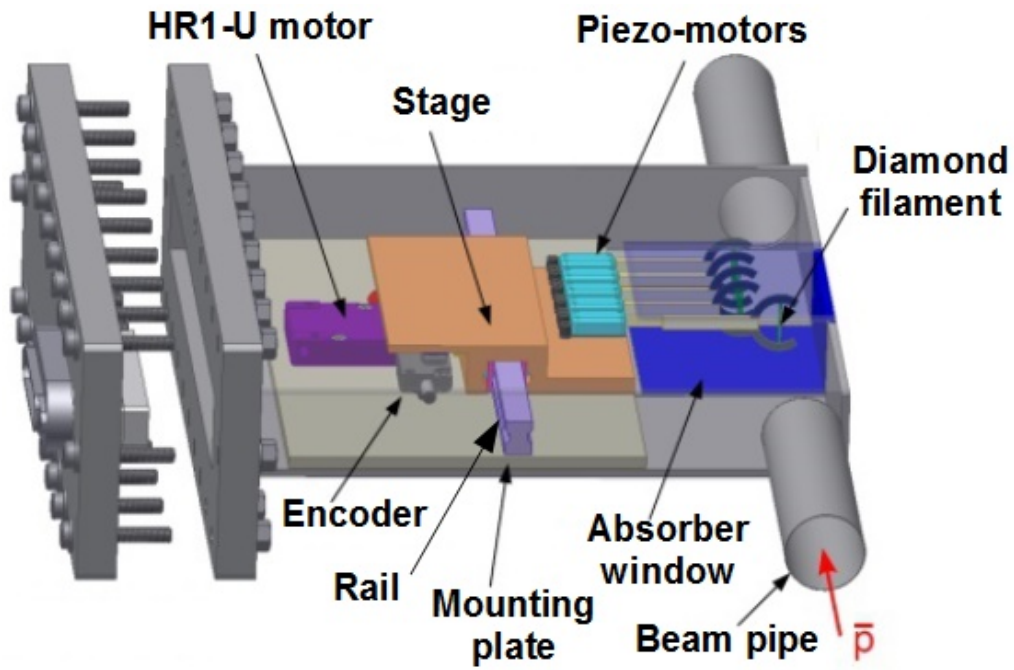
Figure 5.1: Interior of the target chamber with the different components of the moving system for the primary target.
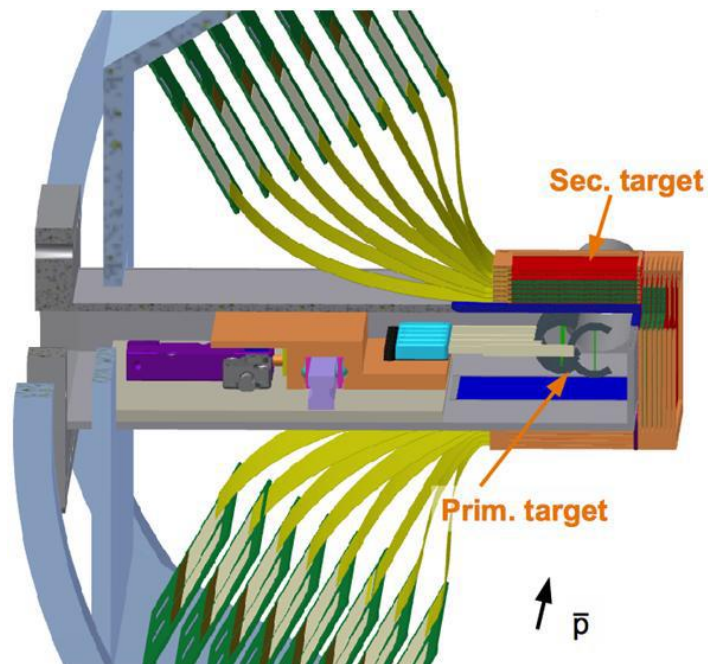
Figure 5.2: Primary and secondary target systems incorporated in the $\overline{\text{P}}$ANDA spectrometer.

In the next sections, a brief description of each component of the setup that handles the primary target will be provided. Furthermore, the tests performed to check the properties of the piezo-motors will be presented. Finally, the mounting and running process of the system will be commented, which includes a detailed description of the calibration procedure of the encoder.

5.1 Description of the components of the system

The components of the system that drives the primary target are, essentially, the following: five piezo-motors to move the primary target, a ceramic motor to displace the stage where the piezo motors are placed, a linear encoder to read the position of the stage and a mounting plate where all the components are fixed. In the next paragraphs a description of each one of the elements of the setup will be given.

Piezo-motors: The piezo-motors are in charge of carrying the primary targets and driving them into the beam by means of an arm that can move forward and backward. They have to be tiny, precise and work correctly under high vacuum and magnetic field conditions. There are not many providers that offer motors with such characteristics. Two piezo-motors from the company PiezoMotor have been selected, the PiezoWave 0.1 N (figure 5.3) and the PiezoLegs (see figure 7.1 of the Appendix). The specifications of the PiezoWave motor provided by the manufacturer can be found in table 7.1 of the Appendix.

Figure 5.3: PiezoWave 0.1N motor[78].

Ceramic motor: The task of this motor is to move the stage that carries the piezo-motors. The HR1-1-U-0 ceramic motor (figure 5.4), designed and manufactured by Nanomotion, is ideal for this goal. By pressing the ceramic fingertip against a ceramic strip a driving force is exerted on the linear stage, creating motion. These motors combine unlimited stroke with high resolution in compact dimensions. The HR1-U is constructed of materials that have been selected and designed for high vacuum compatibility and it is suitable to operation in a 1.5 T to 3 T MRI environment. It has no magnetic materials and no intrinsic magnetic field [79]. The specifications of this motor provided by the manufacturer are listed in table 7.3 of the Appendix.
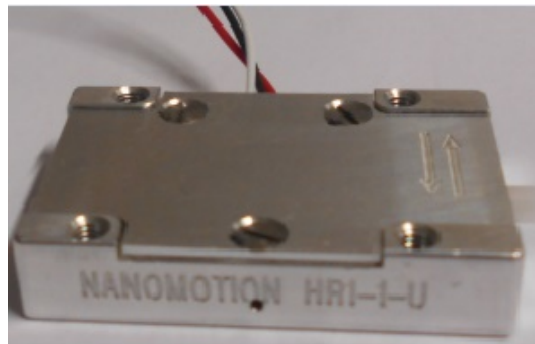
Figure 5.4: HR1-U ceramic motor from Nanomotion [79].

Stage: The stage is the platform on which the piezo-motors are fixed. Its sketch can be seen in figure 7.2 of the Appendix. This stage is screwed on a carriage that slides on a rail by means of rolling bearings allowing to change the position of the piezo-motors and, therefore, of the target with respect to the beam line. The miniature profile rail LLMHS7LA provided by SKF has been selected for this purpose because it allows maximum performance on a minimum of mounting space. In figure 5.5appears the rail with its respective carriage and a sketch that illustrates its reduced dimensions. Although the selected rail is not valid for the $\overline{\mathrm{P}}$ANDA experiment since it is not suitable for vacuum applications, it has been used in our first system prototype to check that the idea of such a movable stage works.
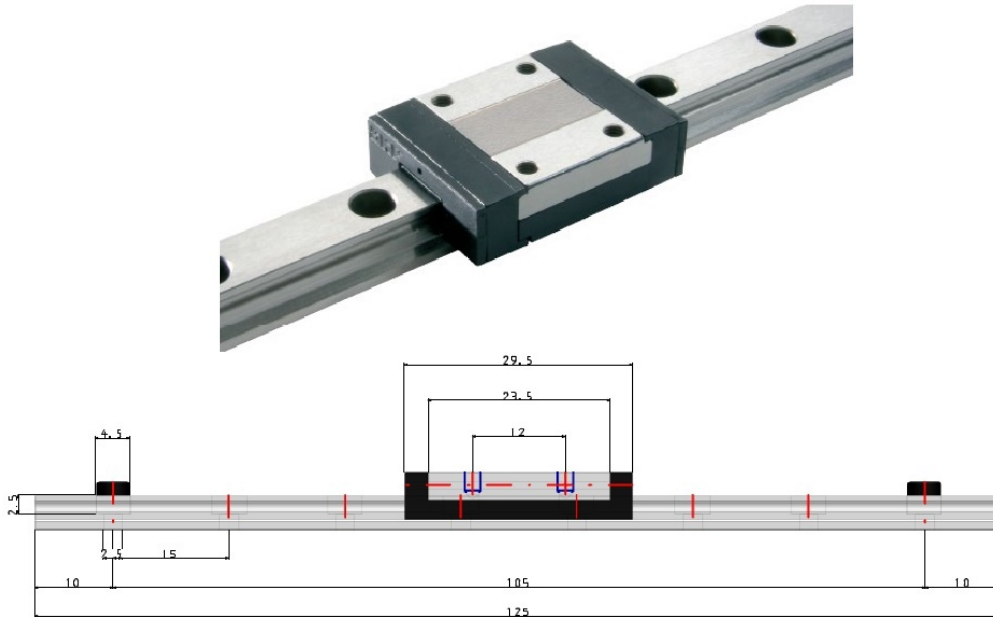
Figure 5.5: SKF miniature profile with its respective carriage and a drawing that shows their dimensions.

Linear encoder: The encoder reads the position of the stage by means of a glass scale situated at the bottom face of the stage. The choice has been the Mercury 1000V sensor (figure 5.6) from MicroE Systems which is very small, easy to align, has a high permorfance and a 10^{-8} Torr vacuum rating [80]. The main features of this are summarized in table 7.2 of the Appendix.

Figure 5.6: Mercury 1000V linear encoder from MicroE Systems [80].

Mounting plate: It is needed to use a base plate to mount all the components of the system on it in order not to perforate the bottom face of the target chamber. Taking into account the dimensions of the chamber and the position of the elements that will be mounted on it, the design of figure 7.3 of the Appendix has been chosen.

Before arranging all the parts of the setup together, the properties of the piezo-motors have been studied and the results will be exposed in the next section.

5.2 Testing the piezo-motors

Until now only the properties of the PiezoWave motor have been tested, the ones of the Piezo-Leg will be checked in the near future. The demo-kit of the PiezoWave 0.1N (figure 5.7) comes with the following components: two motors, one handheld driver, one compact driver, one RS232 interface card, one motor interface card and cables. Additional motors have been ordered for the tests.
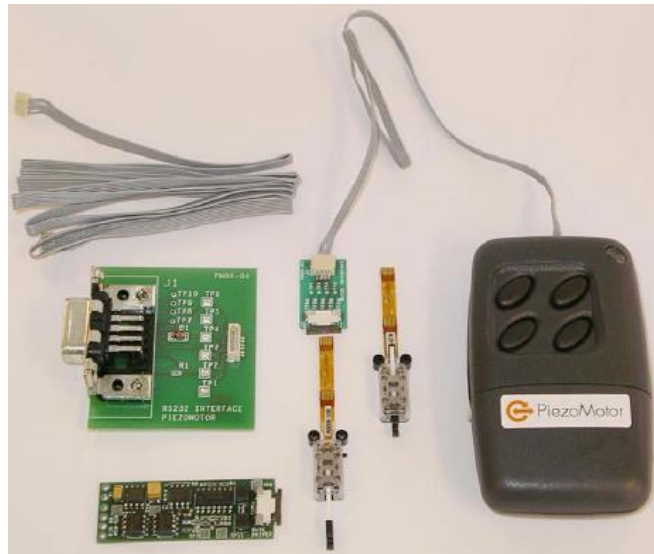
Figure 5.7: Parts in the PiezoWave demo-kit: two motors, one handheld driver, one compact driver, one RS232 interface card, one motor interface card and cables.

The motor can be performed by the handheld driver that gives the possibility to drive the mo-

tor at two selected speeds apart from changing the movement direction. It can also be run by an application for the computer (figure 5.8) which can drive the motor at two different speeds, high and low. The motor will move the selected number of steps with the speed and direction chosen. To use the PC to control the motor the RS232 interface card must be connected to the PC and to the handheld driver via the cable supplied in the demo-kit [81].
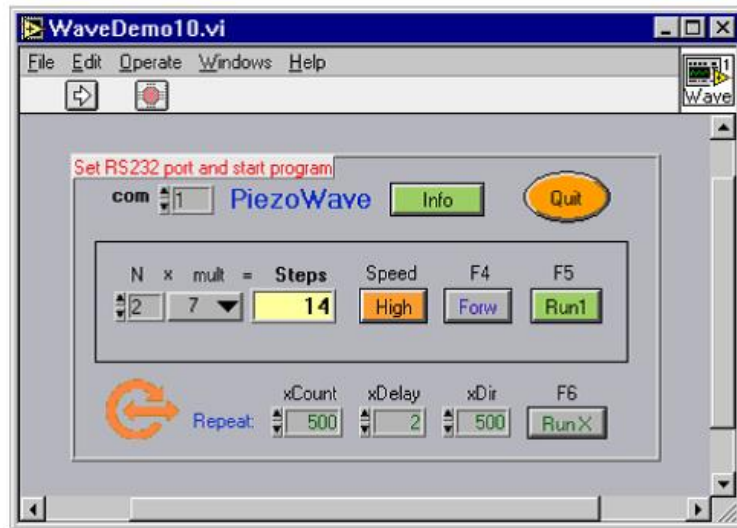
Figure 5.8: PC application to control the motor at high and low speed and for different number of steps.

In the next tests it will be checked that the average step, the maximum stroke, the dynamic force and the holding force of the piezo-motors correspond to the values provided by the manufacturer. These properties have been tested in four different situations: under standard conditions, in vacuum, in a magnetic field and after a radiation test with protons. Furthermore, the gases that they release when exposed to high vacuum will be analyzed.

5.2.1 Performance under standard conditions

It must be checked that the piezo-motors accomplish the features provided by the company. The motor has to be strong enough to move the target with precision. To measure the force a metal structure has been built. As one can see in (figure 5.9), the motor and its respective

scale are fixed on one of the arms of the structure. A thin thread is tied to the arm of the motor and goes through a pulley which is used to reduce the friction. At the end of the thread it is possible to hang weights of different masses. According to the Second Law of Newton, the force that acts on the weights towards the floor is equal to the product of the mass of the object (m) and the gravitational acceleration (g): $\vec{P} = m\vec{g}$ (weight force), where g= 9.8 m/s^2. If the motor can pull the mass hanging from the thread it means that its dynamic force is bigger than the weight force that corresponds to that mass. On the other hand, the holding force refers to the point at which the motor cannot pull the weight but can hold it in equilibrium. Different masses have been attached to the thread and, running the motor with the handheld driver, it has been obtained that the maximum mass that the motor can pull is 14.3 g and the maximum mass that it can hold is 89.8 g. That leads to a dynamic force of approximately 0.14 N and a holding force of 0.88 N.

To check the maximum stroke of the motor its arm has been displaced up to the end position. This has been done with the motor carrying weights and without weights, obtaining that the maximum length does not change. The microscope image of figure 5.10 shows that the maximum stroke corresponds to 8 mm.

Using the application for the PC the average length of one step has been measured. The motor has been driven at high and low velocity selecting each time a different number of steps. The distance traveled by the arm has been then divided by the number of steps, obtaining the length of one single step. Summing all the results and dividing them by the number of measurements the average length of one step has been calculated, turning out to be 0.96 μm.

5.2.2 Performance in vacuum

The primary target system will work under high vacuum conditions at the $\overline{\text{P}}$ANDA experiment so it must be checked that the properties of the motor do not change when it works under such conditions. For that purpose, the same procedures as before have been carried out but this time inside of the vacuum chamber of figure 5.11. Due to the difficulty of reading the position of the arm of the motor with the microscope when the motor is inside the chamber, only the
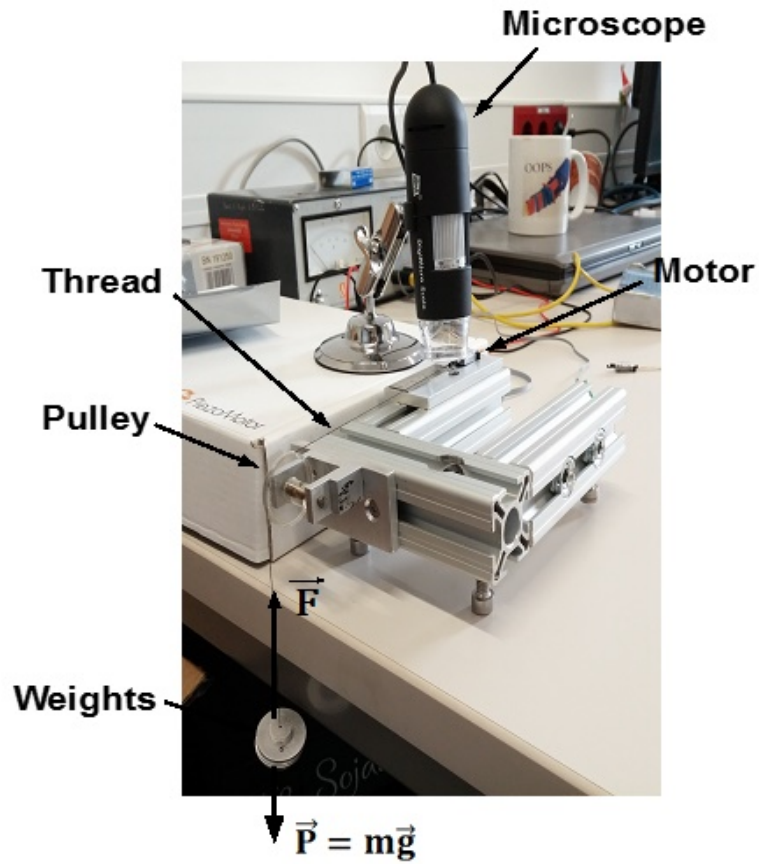
Figure 5.9: Structure constructed to measure the dynamic force of the piezo-motor.
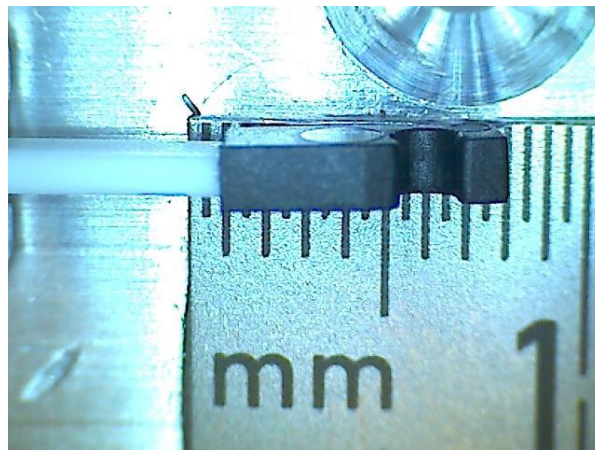
Figure 5.10: Image of the maximum stroke provided by the microscope.

dynamic and holding forces have been measured in this case. Since the chamber was quite small some modifications had to be done in the metal structure to reduce its size so that it fits in the reduced space of the chamber. To measure the strength of the motor a set of thin aluminum weights has been used. After evacuating the chamber a vacuum of 10^{-6} mbar has been reached.

Figure 5.11: View from above of the vacuum chamber with the metal structure inside of it.

It has been observed that the maximum mass that the motor can pull is 15.3 g and the maximum mass that it can hold is 91.8 g. That corresponds to a dynamic force of 0.15 N and a holding force of 0.9 N. Taking into account the errors of the measurements, it is possible to conclude that these values are the same as the ones obtained for the test under standard conditions.

5.2.3 Performance in a magnetic field

Since the primary target will be placed in the interior of the $\overline{\text{P}}$ANDA spectrometer under the presence of a magnetic field, it has to be proved that the performance of the piezo-motors does not change when applying a magnetic field. In order to perform that study, the piezo-motor has been placed inside a U-magnet with a magnetic field of approximately 0.1 T as it is shown in figure 5.12. The magnetic field distribution of the magnet is the one plotted in figure 7.6 of the Appendix.
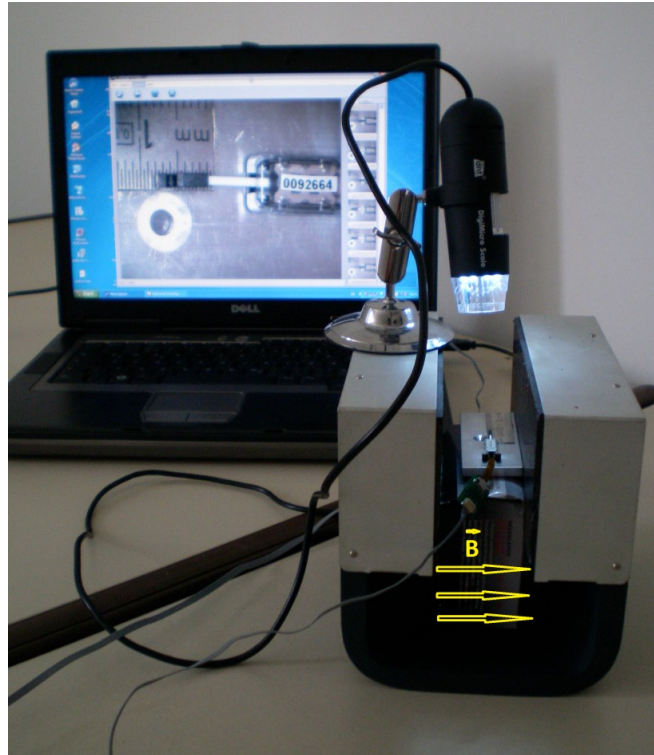
Figure 5.12: Piezo-motor performing in a magnetic field originated by a magnet with U-shape.

Under these conditions the maximum stroke and the average step length have been measured but not the dynamic and holding forces. The values obtained for the maximum stroke and the average step length are 8 mm and 0.94 μm, respectively. Although the magnetic field for the production of hypernuclei inside the $\overline{\text{P}}$ANDA spectrometer will be higher ($\sim$0.5 T), the test performed with the magnet is enough to see that the piezo-motors do not contain materials that could cause problems when working in a magnetic field.

5.2.4 Performance after radiation test at COSY

One of the things that has to be proved is that the piezo-motors do not suffer any damage when being irradiated by a particle beam with comparable characteristics to the ones in $\overline{\text{P}}$ANDA. For that goal a beam test has been carried out in June and July of 2014 at the COSY facility, in particular at the Jessica area marked in figure 5.13. COSY is a cooler synchrotron and stor-

age ring for protons in the momentum range between 600 and 3700 MeV/c (corresponding to energies of 175 and 2880 MeV). It is located at the Institute for Nuclear Physics (IKP) of the Forschungszentrum Jülich (Germany).
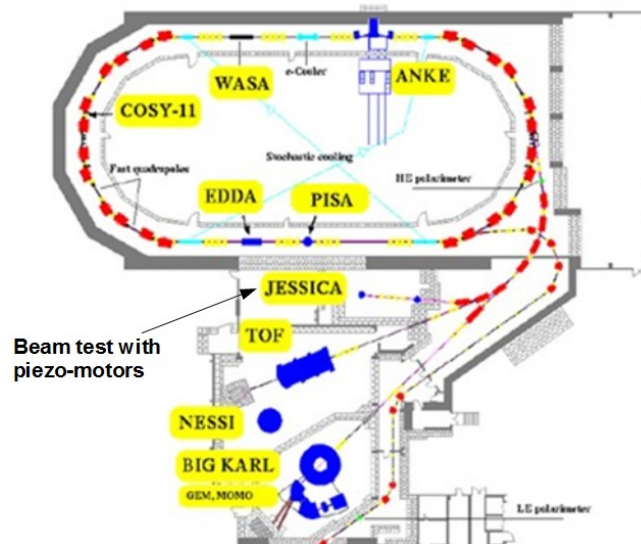
Figure 5.13: COSY facility at IKP.

The experiment has been combined with an irradiation test for the germanium detectors of the experiment. This test needs a thick 5 cm carbon target to produce fast neutrons. On the back of this target two PiezoWave motors have been attached. The beam used for the irradiation is a proton beam with a momentum of 2.78 GeV/c. In figure 5.14 one can see a photo of the whole setup and a zoomed image of the piezo-motors fixed to the back of the carbon target. For the irradiation of the piezo-motors only the target was important, the other components were used for the irradiation test of the germanium detector.

The proton beam has a two-dimensional gaussian profile with a σ of 13.6 mm. The total number of beam protons during the whole measurement is $N_p = 4 \cdot 10^{13}$ p, which corresponds approximately to the number of anti-protons accumulated in 50 days at $\overline{P}ANDA$. Calculating the two-dimensional integral of the gaussian beam over the area of the piezo-motor results in a fraction of 7.3% of the complete beam which hit one of the piezo-motor. Roughly 10% of the

protons interact in the thick carbon target. Discounting this 10% one can calculate the total number of protons passing through a piezo-motor as $n_p = 0.073 \times 0.9 \times N_p = 2.6 \cdot 10^{12}$ p. The surface of a piezo-motor is $A = 0.98 \ cm^2$, what leads to a proton areal density of $N = n_p \times A \approx 2.6 \cdot 10^{12} p/cm^2$.

At $\overline{\text{P}}$ANDA, the motors will be put at a distance of typically $3\,\text{cm}$ from the primary interaction point. The surface of about $0.5\,\text{cm}^2$ pointing to the target corresponds to about 1/200 of the solid angle. With a typical multiplicity at $\overline{\text{P}}$ANDA of about 6 and an interaction rate of $4 \cdot 10^6 \text{s}^{-1}$ this results in about $1 \cdot 10^{12}$ charged particles hitting a motor during a running period of 4 months. Thus the conditions achieved during the test at COSY corresponds roughly to the running period at $\overline{\text{P}}$ANDA.
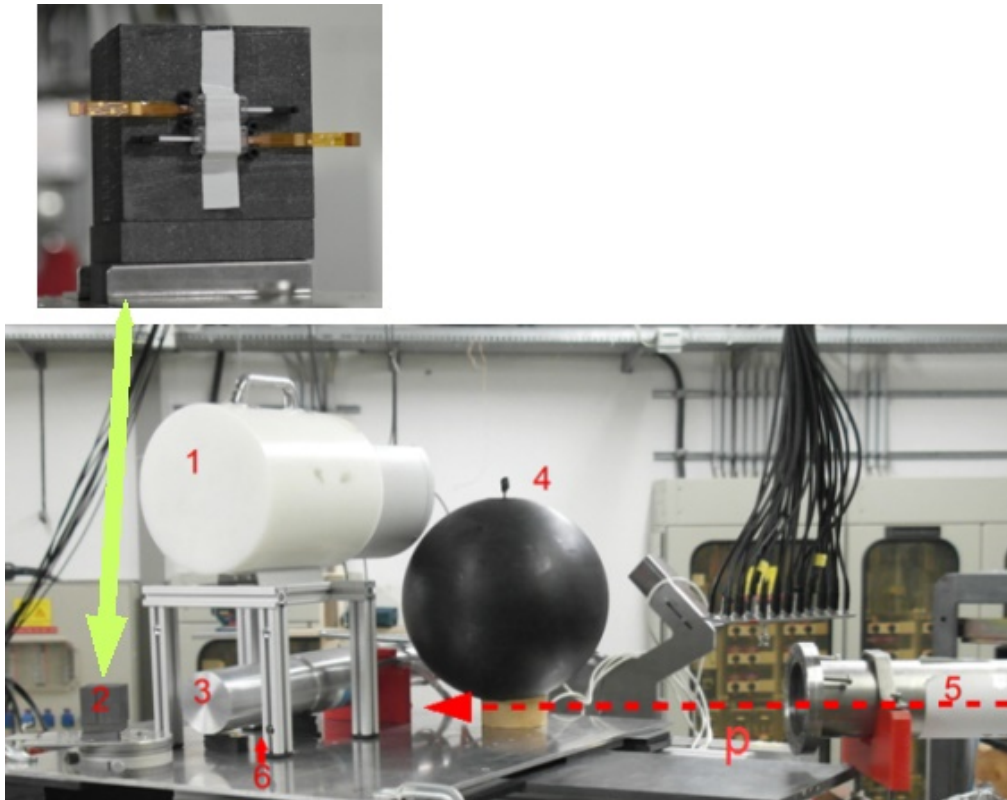
Figure 5.14: Experimental setup. 1: Active neutron detector. 2: Target. 3: Germanium detector. 4: Passive neutron detector. 5: Beam pipe. 6: ^{60}Co source.

After the irradiation all the properties of the motors have been tested again under the same

conditions as in 5.2.1 and following the same procedures. This measurement resulted in a dynamic force of 0.14 N, a holding force of 0.87 N, a maximum stroke of 8 mm and an average step length of 0.95 μm. This indicates that the performance of the piezo-motor has not been affected by the radiation test at COSY and, therefore, the properties of the piezo-motors would neither be worse in the $\overline{\text{P}}$ANDA experiment.

5.2.5 Summary of the results

The previous tests carried out on the motors have revealed that vacuum, the presence of a magnetic field and the interaction with a beam of particles with comparable characteristics to the ones at $\overline{\text{P}}$ANDA do not affect the performance of the piezo-motors. In table 5.1 all the values obtained experimentally for the tested features of the motors are compiled.

Features	Manufacturer	Standard Conditions	Vacuum	Magnetic Field	After radiation test
Stroke maximum	$8\ mm$	$8\ mm$	. . .	$8\ mm$	$8\ mm$
Average step	$0.5 - 1.0\ \mu m$	$0.96\ \mu m$	. . .	$0.94\ \mu m$	$0.95\ \mu m$
Dynamic force	$0.1\ N$	$0.14\ N$	$0.15\ N$	. . .	$0.14\ N$
Holding force	$0.3\ N$	$0.88\ N$	$0.9\ N$	. . .	$0.87\ N$

Table 5.1: Results of the tests performed on the motors compared to the values given by the manufacturer.

Taking into account that the measurements have not been carried out with high precision, it can be concluded that the results obtained from the experiments are compatible with the specifications provided by the company, except for the holding force which is much bigger. Therefore, it has been checked that the PiezoWave motors are suitable for the $\overline{\text{P}}$ANDA experiment.

5.2.6 Outgassing

When materials are under vacuum conditions they release residual gases. The piezo-motors have been submitted to high vacuum (10^{-9} mbar) and the concentration of the elements that appear in the vacuum chamber has been measured. To reach this goal a Residual Gas Analyzer (RGA) together with a set of vacuum pumps have been used as it is shown in the schema of figure 5.15. The different parts of the real setup can be seen in figure 5.16.
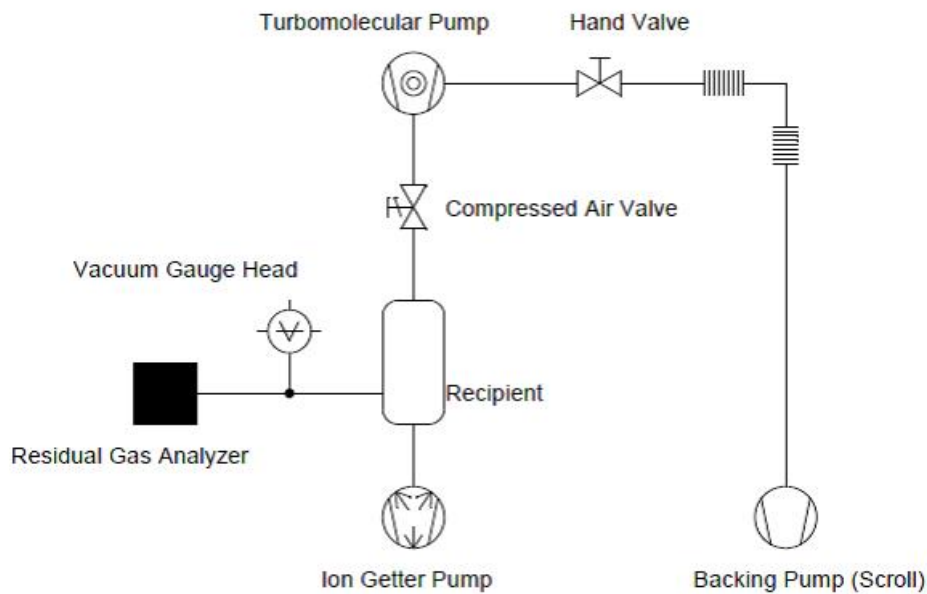
Figure 5.15: Schematic drawing of the experimental setup to measure the residual gases that the piezo-motors release.

Turbomolecular pumps, with a design similar to that of a turbine, belong to the category of kinetic vacuum pumps and are used to obtain and maintain high vacuum. The pumping effect of an arrangement consisting of rotor and stator blades is based upon the transfer of impulses from the rapidly rotating blades to the gas molecules being pumped. Molecules that collide with the blades are absorbed there and leave the blades again after a certain period of time [82]. Ion getter pumps capture and hold gas molecules by converting them into solid compounds and binding them in the pump [83]. Scroll backing pumps consist of two or more Archimedes
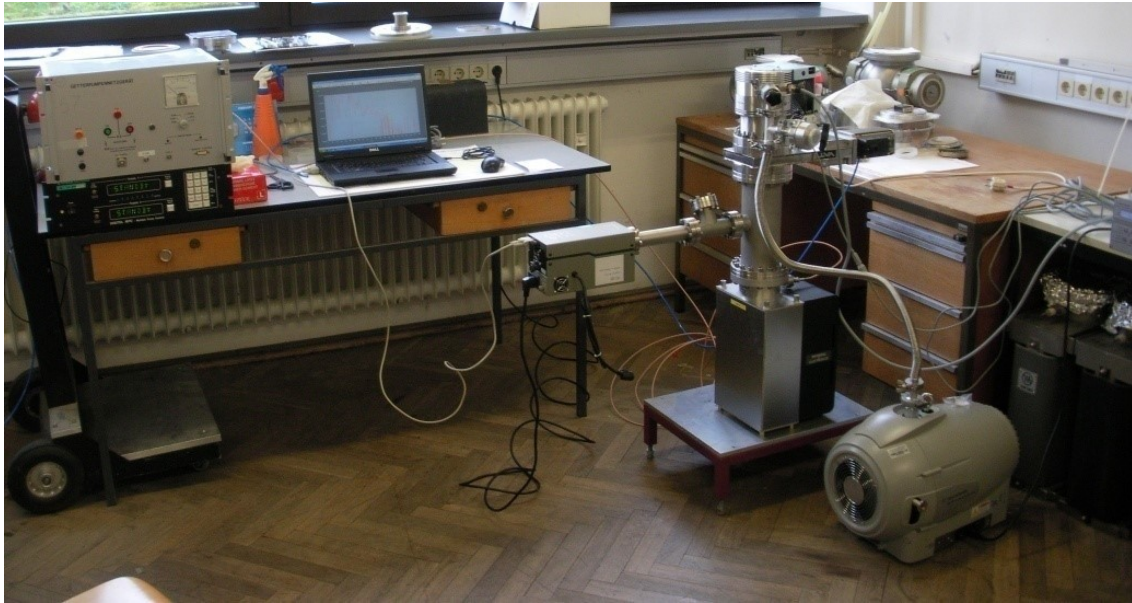
Figure 5.16: Experimental setup to measure residual gasses in high vacuum.

spirals engaging each other. The vacuum is generated by reducing the volume of the pockets and compressing gases from the outside towards the inside thereby pumping the gases [84]. The Residual Gas Analyzer RGA 200 of figure 5.17 is a quadrupole mass spectrometer that covers mass ranges from 1 to 200 amu (atomic mass units) and is intended to be used for the analysis of the gasses present in high and ultra-high vacuum by ionizing some of the gas molecules (positive ions), separating the resulting ions according to their respective masses and measuring the ion currents at each mass. The RGA's resolution is sufficient to clearly distinguish peaks that are 1 amu apart [85]. The recipient is the chamber where vacuum is generated and in which the components that have to be analyzed are placed.

First of all, the gas composition of the vacuum chamber when it was empty has been measured to see which molecules are already present before we introduce the different elements whose contamination has to be measured. Afterwards, four different analysis have been carried out: 1. Complete piezo-motor. 2. Piezo-motor without plastic housing. 3. Teflon ring. 4. Two complete piezo-motors plus one piezo-motor without plastic housing plus one complete motor with the connection cable plus a teflon ring. The pieces have been inserted in the chamber

Figure 5.17: Residual Gas Analyzer RGA 200.

separately first and later all together as in figure 5.18. Before placing the components inside the chamber one has to put talc-free gloves on and clean the elements carefully with acetone. In order to pollute the chamber as less as possible, a long metallic peg has been used to place the objects onto the bottom of the chamber.
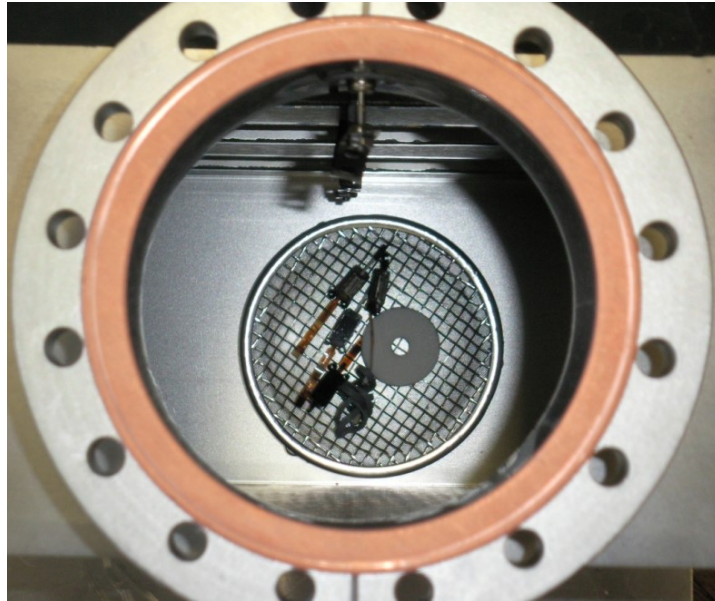
Figure 5.18: Vacuum chamber containing the teflon ring, two complete piezo-motors, one piezo-motor without plastic housing and one complete piezo-motor with the connection cable.
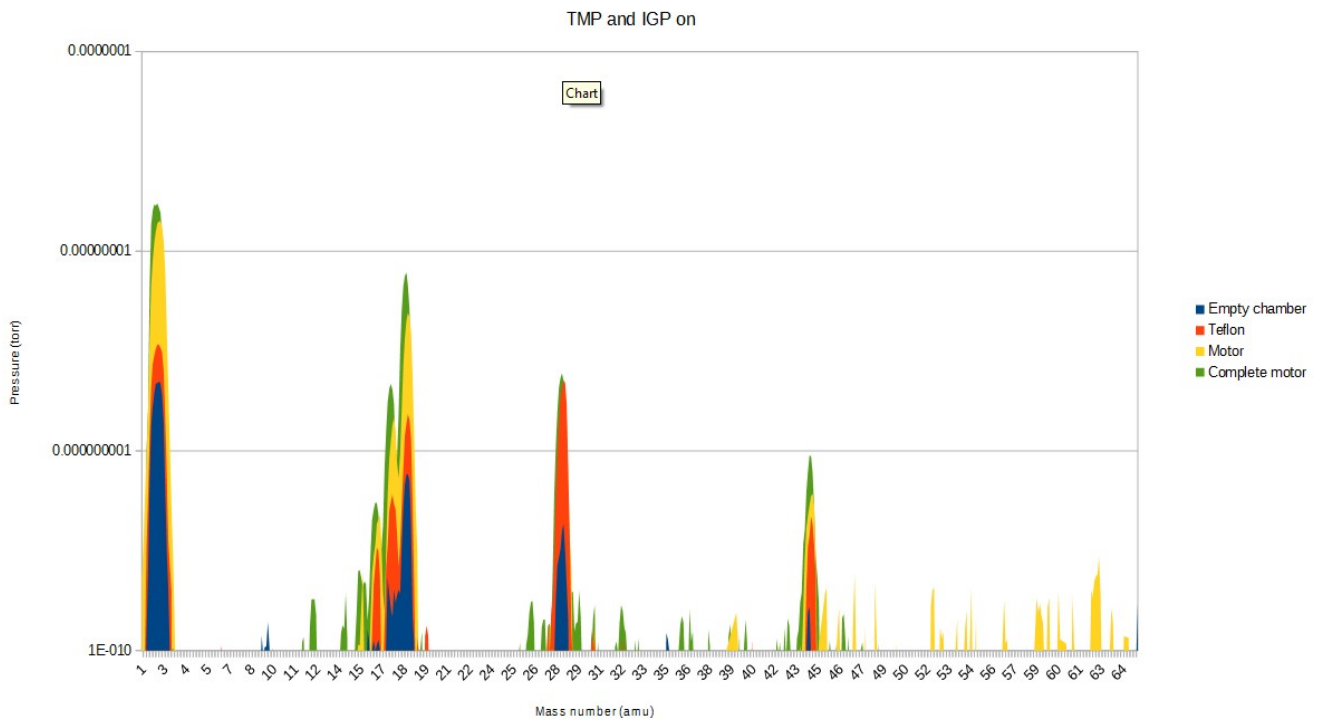
Figure 5.19: Mass spectra. Blue: empty chamber. Red: Teflon ring. Yellow: motor without plastic housing. Green: complete motor.

56

The mass spectra (partial pressure vs. mass number) obtained for the empty chamber and for each of the components have been plotted in a single graph (figure 5.19) so that the results can be easily compared. One can clearly distinguish four significant peaks in all the cases, that correspond to the next elements: hydrogen H_2 (2 amu); water H_2O (18 amu); nitrogen N_2 or carbon monoxide CO (28 amu) and carbon dioxide CO_2 (44 amu). However, in every vacuum system detectable amounts of these species appear so the components that have been studied do not release other gases than the typical ones. As expected, the concentration of the elements is higher for the complete motor and lower for the empty chamber. Removing the plastic housing of the motor does not make a big difference since the intensity of the peaks are practically equal.

Once that the properties of the piezo-motors have been studied, the only thing missing is to mount all the components of the moving system for the primary target and set it in motion. That will be treated in the next section.

5.3 Arrangement of the components

The procedure followed to arrange all the parts of the setup together and drive the stage will be described in this section. The methods used for the right calibration of the encoder will be exposed in detail.

5.3.1 Calibrating the sensor

The M1000V encoder and the scale have to be aligned so that the sensor can read over the whole length of the scale. The system has been calibrated by using first the SmartPrecision Alignment Tool and then the SmartPrecision Software to check that the first alignment was done correctly.

First of all, one has to attach the encoder to the mounting plate with screws. Later one has to connect the M1000V to the SmartPrecision Alignment Tool and this one to the Computer In-

terface Adapter which is connected to the power supply. The adjustment of the scale position with respect to the sensor is done easily with the SmartPrecision Alignment Tool as illustrated in figure 5.20. The red, yellow, or green LED will light depending on sensor alignment. Making sure that the grating surface of the scale faces the sensor and that the distance between them is not bigger than 1 mm because otherwise the intensity of the signal would be too low, the scale has to be moved slowly (using talc-free gloves to handle it) by allowing it to slide on the mounting surface of the stage until the green LED is illuminated. Optimal alignment will be displayed as a "Bright Green" LED. When alignment is completed, one has to fix the scale by using epoxy glue or two sided adhesive tape. To see if the calibration was done properly one has to confirm that the "green" LED remains on over the full range of motion by sliding the scale past the sensor [86].
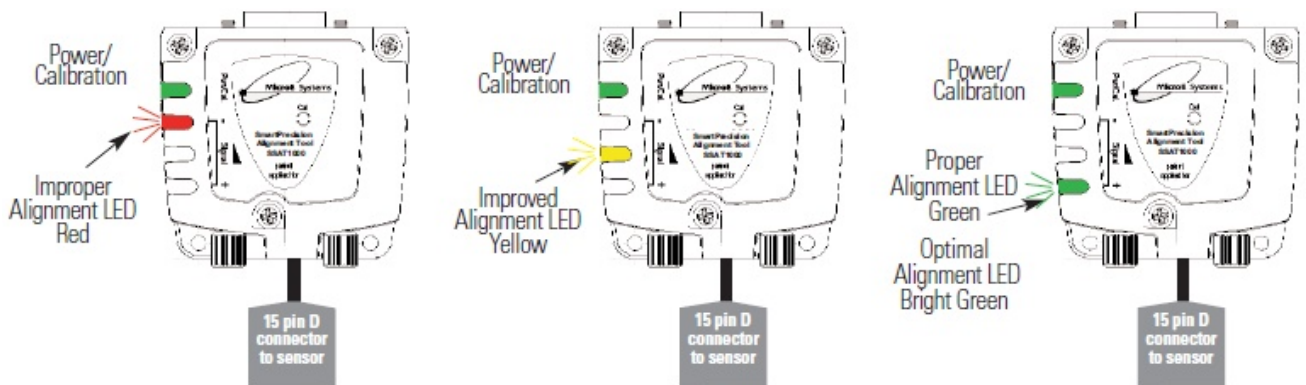
Figure 5.20: SmartPrecision Alignment Tool for calibrating the encoder.

To check that the alignment with the SmartPrecision Alignment Tool was done successfully the SmartPrecision Software has been used. One has to connect the Computer Interface Adapter to the PC and slide the scale past the sensor. If the scale is properly positioned with respect to the sensor, the arrow of the signal level indicator that appears in the screen will be pointing the green area. The upper the arrow is, the better is the alignment (see [86]).

After fixing the scale to the stage aligned with the sensor, the other parts of the system have been mounted and the stage has been driven by running the HR1-U motor as will be explained

in the following part.

5.3.2 Mounting and driving the stage

All the parts that comprise the system have been fixed to the base plate. After mounting everything, some modifications had to be done so that all the pieces fit. The finger tip of the motor was too low with respect to the ceramic bar so a plate had to be placed under it to bring it to a higher position. Furthermore, a stopper for the stage had to be located on the rail so that the travel length of the carriage does not exceed the length of the ceramic driving bar. The sketches of both pieces appear in Figures 7.4 and 7.5 of the Appendix. Moreover, since the arm of the piezo-motor was too short to reach the beam line, a hook like the one of figure 5.21 has been designed as prolongation of the arm.
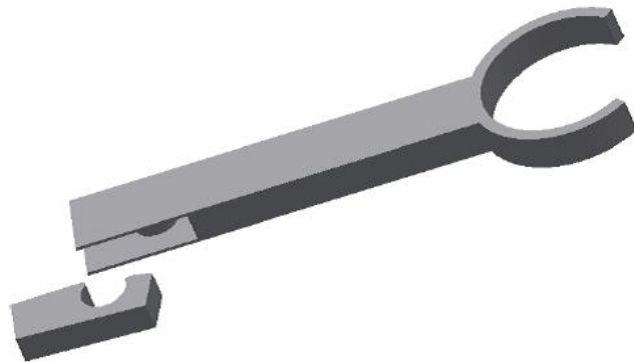
Figure 5.21: Hook designed as prolongation of the piezo-motor arm.

After applying the modifications, all the parts have been mounted again, this time successfully obtaining the result of figure 5.22.
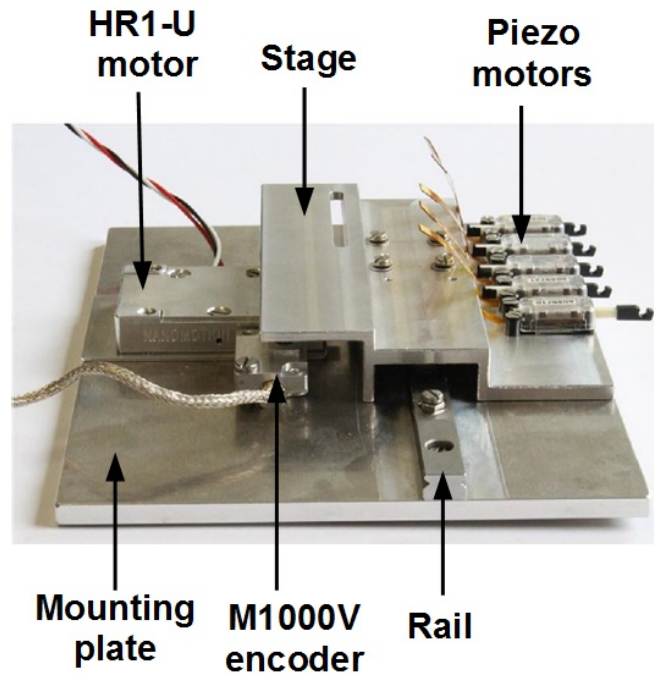
Figure 5.22: System with all the components.

With all the components of the setup placed in the right position the only thing missing is to set the stage in motion by running the ceramic motor. For that goal, the AB1A single axis driver has been used. The driver works as a velocity amplifier and can receive a signal from an external joystick, providing motion to the motor in a continuous mode [87]. In figure 5.24 one can see how all the components are connected to move the stage and read its position. The HR1 motor is connected to the driver box and this one to the joystick and to a power supply. For a better understanding of the system a block diagram that shows how the different components are connected is represented in figure 5.23. Until now, the motor has only been run manually with the help of the joystick. The next step will be to drive the motor with the controller board DMC-4113 and its respective software GalilTools.
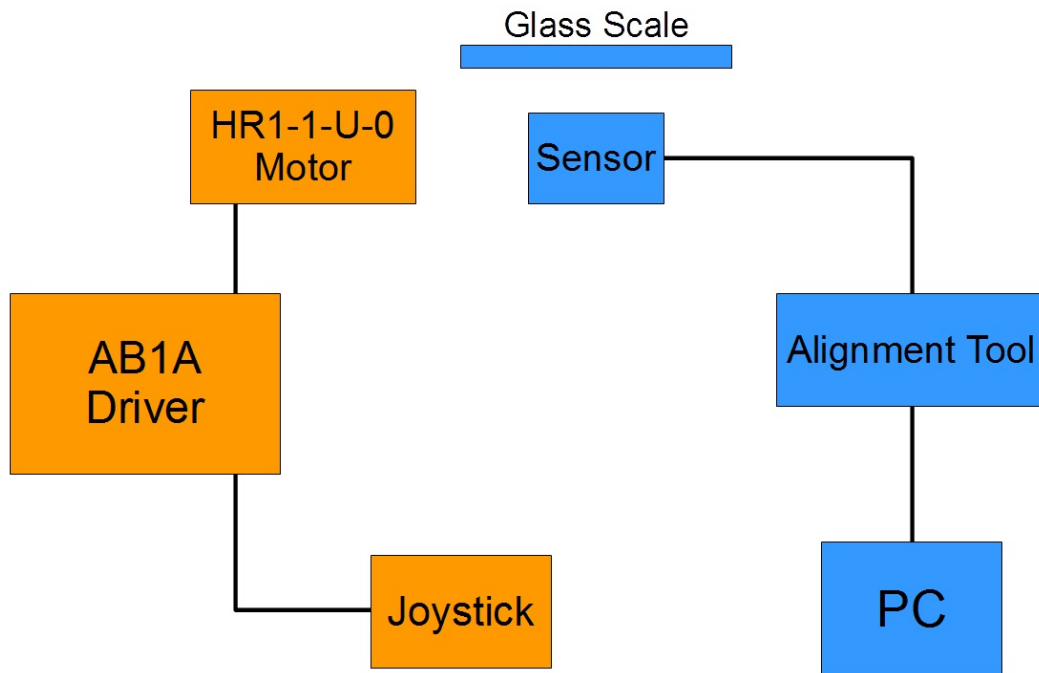
Figure 5.23: Block diagram that shows how the different components of the system are connected.
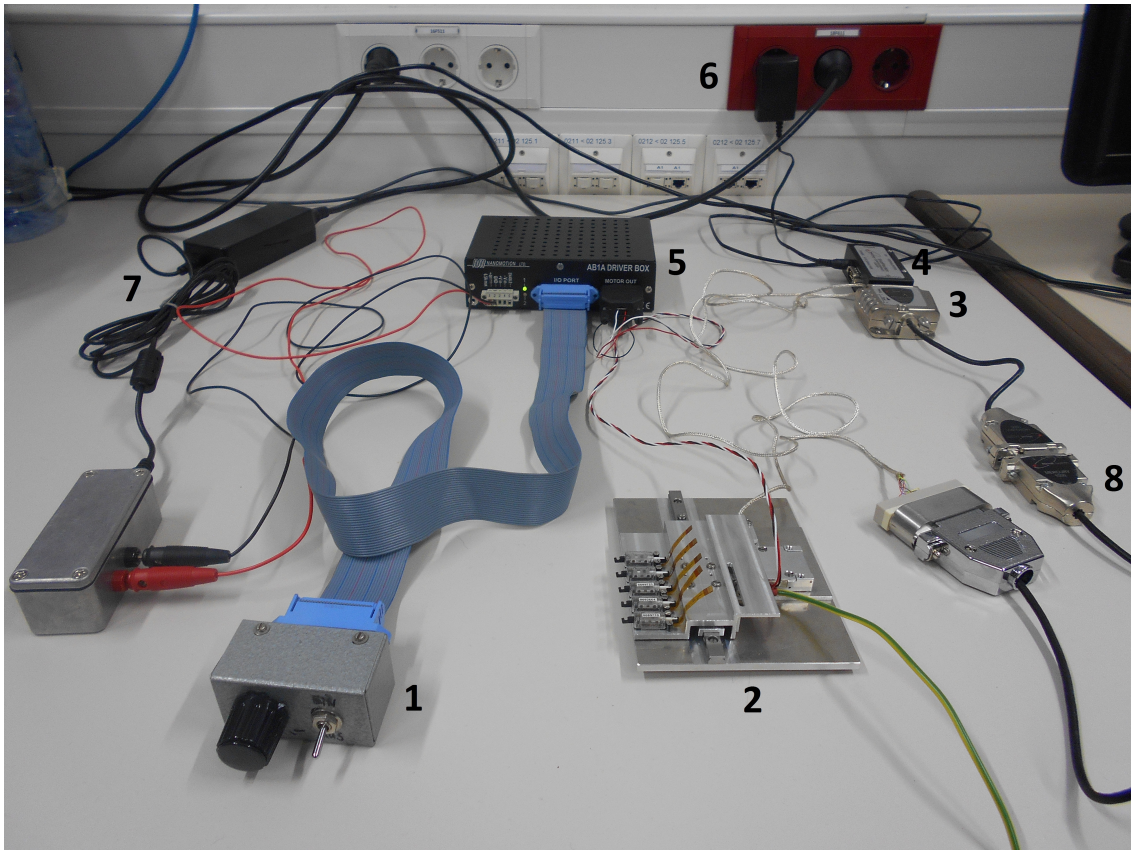
Figure 5.24: 1: Joystick for controlling the HR1 motor. 2: Stage. 3: SmartPrecision Alignment Tool SS-AT 1000. 4: Computer Interface Adapter RS232. 5: AB1A Driver Box. 6: Power supply for the encoder. 7: Power supply for the HR1 motor. 8: Controller Interface Cable.

6 Summary

In summary, in the present work, the characteristics of the $\overline{\mathrm{P}}$ANDA experiment have been presented as well as the designs and tests that have been carried out in order to optimize the primary target system for the creation of double lambda hypernuclei. The material for the primary target has been selected considering that the Ξ^- production rate must be as high as possible, the beam losses kept low and the hadronic background minimal. In addition, its thermal conductivity must be high so that it can resist high temperatures without breaking. Taking into account these requirements ^{12}C, ^{28}Si and ^{48}Ti have been considered as possible target materials. As a first target prototype a diamond filament with a thickness of 3 μm and a width of 100 μm has been produced and irradiated by a beam of electrons. After the radiation test a black spot has appeared in the middle of the filament due to the collisions of the electrons. However, the comparison of the operating conditions of this experiment with the ones of $\overline{\mathrm{P}}$ANDA indicates that this target is feasible. A second primary target prototype made of pitch based carbon fibers DIALEAD is foreseen for future studies.

Furthermore, a devoted target chamber has been designed with a window surrounding the area in which the target is located. The study of the deformation of the different window foils when the chamber is pumped shows that this model works for some of the materials. However, with this prototype one would have to increase the distance between the primary and secondary targets to conserve the 20 mm free space needed inside the chamber what would reduce the efficiency of the Ξ^- absorption. That leads to a new design with the secondary target absorbers incorporated directly in the chamber. A system that permits to move and replace the primary target has been designed. The setup consists of five tiny piezo-motors that

displace the target and a stage driven by a ceramic motor that allows to change the position of the piezo-motors with respect to the beam line. The properties of the piezo-motors have been checked under standard conditions, in vacuum, in a magnetic field and after a radiation test, concluding that they are suitable for $\overline{\text{P}}$ANDA. Moreover, the analysis of the residual gases released by the piezo-motors in high vacuum shows that they do not release molecules that could interfere with the experiment. The sensor that reads the position of the stage has been aligned successfully with respect to the glass scale. Finally, all the parts of the system have been arranged together and the stage has been set in motion by running the HR1-U motor manually with a joystick. The next step will be to develop an automated setup to handle the target frame.

In conclusion, several features of the primary target system of $\overline{\text{P}}$ANDA were successfully studied in this master thesis.

7 Appendix

To drive the primary target into the beam two motors have been selected as candidates, the PiezoWave 0.1N and the PiezoLeg. The characteristics of the first one have been already checked and the second one will be tested soon. In Figure 7.1 one can see the PiezoLeg with the specifications provided by the manufacturer.

Weight: 23 g
Size: 22 mm x 19.3 mm x 10.8 mm
Maximum speed: 0-15 mm/s
Stroke max: 80 mm
Average step: 4 µm
Dynamic force: 6.5 N
Holding force: 7 N

Figure 7.1: PiezoLeg motor plus the specifications provided by the manufacturer [88].

The specifications provided by the companies for the PiezoWave motor, the encoder and the ceramic motor are listed in the tables below.

Size	14.0 mm (L) x 7.2 mm (W) x 4.4 mm (H)
Weight	0.5 g
Maximum speed	50-100 mm/s
Stroke maximum	8 mm
Average step	0.5-1.0 μm
Dynamic force	0.1 N
Holding force	0.3 N

Table 7.1: Main properties of the PiezoWave motor.

Size	20.6 mm (L) x 12.7 mm (W) x 8.4 mm (H)
Weight	1.6 g
Resolution	20 μm
Accuracy	$\pm$ 1 μm

Table 7.2: Main properties of the M1000 encoder.

Size	40.5 mm (L) x 25.7 mm (W) x 8 mm (H)
Weight	0.5 g
Maximum velocity	250 mm/s
Dynamic stall force	3.5-4.5 N
Average step	0.5-1.0 μm
Vacuum level	10^{-10} Torr

Table 7.3: Main properties of the HR1-U motor.

The detailed sketches of the different parts of the primary target system are shown under these lines. In figures 7.2, 7.5, 7.4 and 7.3 appear the dimensions of the stage, the mounting plate, the plate for the HR1 motor and the stopper for the rail, respectively.

The magnetic field distribution of the magnet used to test the magnetic properties of the piezo-motor is plotted in figure 7.6.
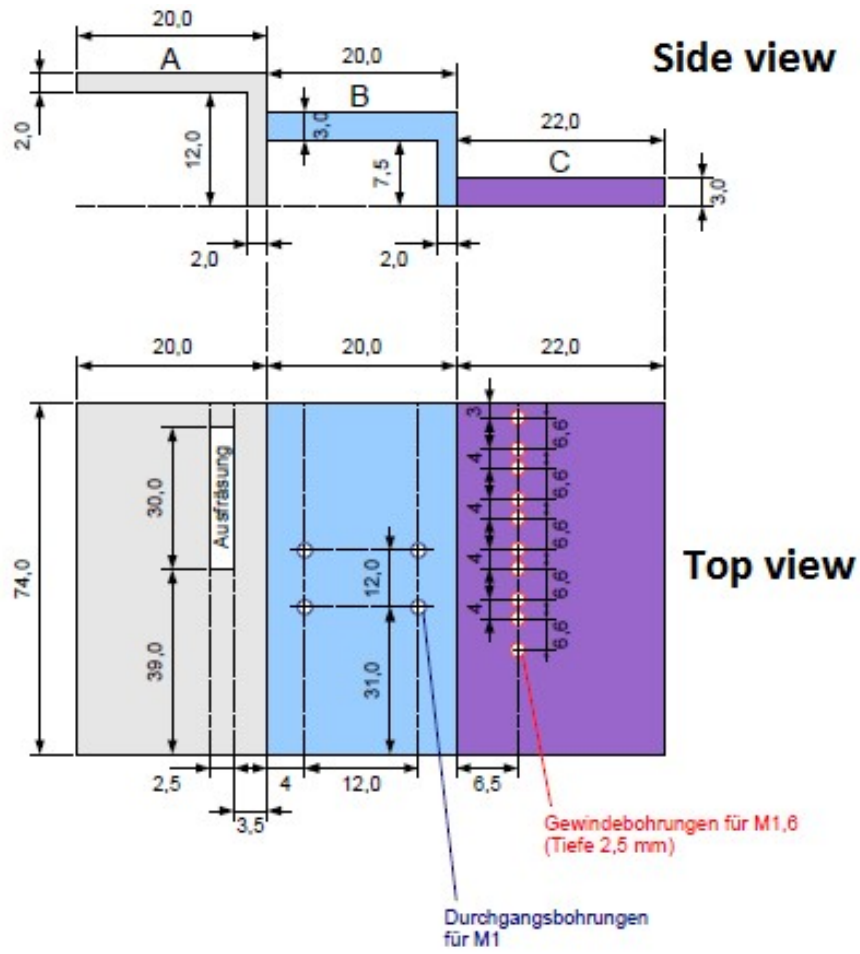
Figure 7.2: Sketch of the movable stage for the piezo-motors.
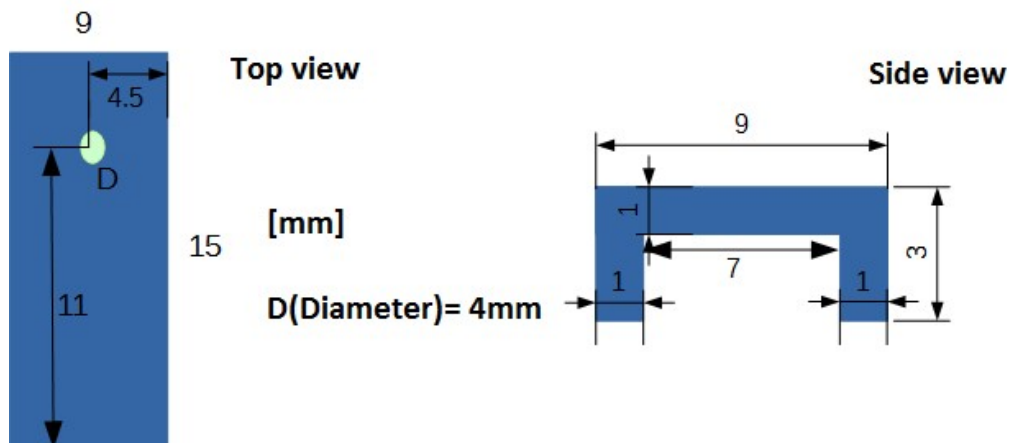
Figure 7.3: Stopper for the rail.

Figure 7.4: Plate to place the motor higher.

Figure 7.5: Mounting plate.

68
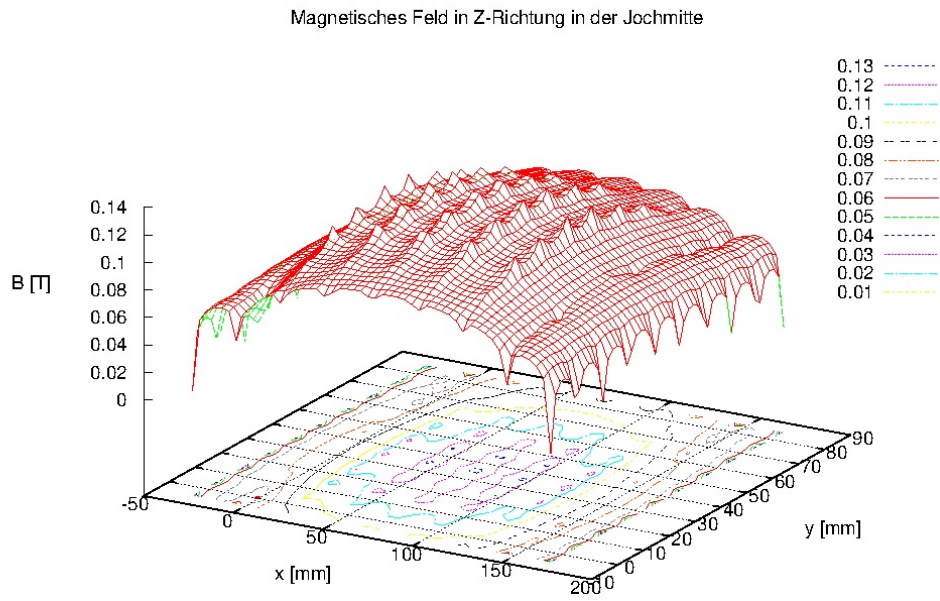
Figure 7.6: Magnetic field distribution of the magnet [89].

List of Figures

List of Tables

Bibliography

[1] J. BERINGER ET AL.: *Particle Data Group, Λ Baryon.* `https://pdg.lbl.gov/` `2012/tables/rpp2012-tab-baryons-Lambda.pdf`, 2012

[2] PROF.DR.JOSEF POCHODZALLA: *Beyond the conventional nuclear chart: hyperons and antihyperons in nuclear systems.* `https://fias.uni-frankfurt.de/` `fileadmin/fias/common/PDF/Colloquium/fias_semi081113.pdf`, 2008

[3] KERNFYSISCH VERSNELLER INSTITUUT, UNIVERSITY OF GRONINGEN (NETHER-LANDS): *Hadron Physics with Anti-protons: The $\overline{P}$ANDA Experiment at FAIR.* `http:` `//www.slac.stanford.edu/econf/C070910/PDF/Messchendorp.pdf`, 2007

[4] A. SANCHEZ LORENTE: *Feasibility study of performing high precision gamma spectroscopy of ΛΛ hypernuclei in the $\overline{P}$ANDA experiment*, Diss.

[5] CHESTON, W. ; PRIMAKOFF, H.: Nonmesonic bound V-particle decay. In: *Phys. Rev.* 92 (1953), Dec, Nr. 6, S. 1537

[6] FETISOV, V. N. ; KOZLOV, M. I. ; LEBEDEV, A. I.: On the possibility of hypernucleus production by high energy protons and electrons. In: *Physics Letters B* 38 (1972), Nr. 3, 129 - 131. `http://dx.doi.org/DOI:10.1016/0370-2693(72)90030-5`. – DOI DOI: 10.1016/0370–2693(72)90030–5. – ISSN 0370–2693

[7] DOVER, C. B. ; LUDEKING, L. ; WALKER, G. E.: Hypernuclear physics with pions.

In: *Phys. Rev. C* 22 (1980), Nov, Nr. 5, S. 2073–2093. `http://dx.doi.org/10.1103/PhysRevC.22.2073`. – DOI 10.1103/PhysRevC.22.2073

[8] BERNSTEIN, A. M. ; DONNELLY, T. W. ; EPSTEIN, G. N.: Production of hypernuclei by the ([gamma], K) reaction. In: *Nuclear Physics A* 358 (1981), 195 - 202. `http://dx.doi.org/DOI:10.1016/0375-9474(81)90317-1`. – DOI DOI: 10.1016/0375–9474(81)90317–1. – ISSN 0375–9474

[9] HSIAO, Shian S. ; COTANCH, Stephen R.: Hypernuclear excitation through kaon photoproduction. In: *Phys. Rev. C* 28 (1983), Oct, Nr. 4, S. 1668–1678. `http://dx.doi.org/10.1103/PhysRevC.28.1668`. – DOI 10.1103/PhysRevC.28.1668

[10] COHEN, Joseph: (e, e'K+) reaction on nuclei. In: *Physics Letters B* 153 (1985), Nr. 6, 367 - 371. `http://dx.doi.org/DOI:10.1016/0370-2693(85)90474-5`. – DOI DOI: 10.1016/0370–2693(85)90474–5. – ISSN 0370–2693

[11] CRUSSARD, J. ; MORELLET, D.: Emission probable d'un fragment nucléaire contenant une particule V^0. In: *Comptes Rendus* 236 (1953), S. 64

[12] DANYSZ, M. ; PNIEWSKI, J.: Delayed Disintegration of a Heavy Nuclear Fragment: I. In: *Phil. Mag.* 44 (1953), S. 348

[13] TIDMAN, D.A. ; DAVIS, G. ; HERZ, A.J. ; TENNENT, R.M.: Delayed Disintegration of a Heavy Nuclear Fragment: II. In: *Phil. Mag.* 44 (1953), S. 350

[14] POWELL, C.F. ; FERTEL, G.E.F.: Energy of High-Velocity Neutrons by the Photographic Method. In: *Nature* 144 (1939), S. 115

[15] FRANK, F. C. ; PERKINS, D. H.: Cecil Frank Powell. 1903-1969. In: *Biographical Memoirs of Fellows of the Royal Society* 17 (1971), 541–563. `http://www.jstor.org/stable/769719`. – ISSN 00804606

[16] OCCHIALINI, G.P.S. ; POWELL, C.F.: Observations on the production of mesons by cosmic radiation. In: *Nature* 162 (1948), S. 168

[17] CIOK, P. ; DANYSZ, M. ; GIERULA, J.: Delayed decay of heavy fragments ejected from cosmic ray stars. In: *Nuovo Cimento* 11 (1954), S. 436

[18] ROCHESTER, G.D. ; BUTLER, C.C.: Evidence for the existance of new unstable elementary particles. In: *Nature* 160 (1947), S. 855

[19] BONETTI, A. ; SETTI, R. L. ; PANETTI, M. ; SCARSI, L. ; TOMASI, G.: In: *Nuovo Cimento* 11 (1954), 210 S.

[20] FRY, W.F. ; SCHNEPS, J. ; SWAMI, M.S.: Disintegration of Hyperfragments. In: *Phys. Rev.* 99 (1955), Sep, Nr. 5, S. 1561–1572. `http://dx.doi.org/10.1103/PhysRev.99.1561`. – DOI 10.1103/PhysRev.99.1561

[21] SORRELS, J.D. ; TRILLING, G.H. ; LEIGHTON, R.B.: Λ^0-Fragment Decay in a Cloud Chamber. In: *Phys. Rev.* 100 (1955), Dec, Nr. 5, S. 1484–1486. `http://dx.doi.org/10.1103/PhysRev.100.1484`. – DOI 10.1103/PhysRev.100.1484

[22] FRODESEN, A. G. ; RÃ¸E, T. ; SKJEGGESTAD, O.: A systematic study of hypernuclei from Σ- captures in nuclear emulsions. In: *Nuclear Physics* 68 (1965), Nr. 3, 575 - 581. `http://dx.doi.org/DOI:10.1016/0029-5582(65)90391-3`. – DOI DOI: 10.1016/0029–5582(65)90391–3. – ISSN 0029–5582

[23] FRY, W. F. ; SCHNEPS, J. ; SWAMI, M. S.: Disintegration of Hyperfragments. II. In: *Phys. Rev.* 101 (1956), Mar, Nr. 5, S. 1526–1535. `http://dx.doi.org/10.1103/PhysRev.101.1526`. – DOI 10.1103/PhysRev.101.1526

[24] LEMONNE, J. ; MAYEUR, C. ; SACTON, J. ; DAVIS, D.H. ; GARBUTT, D.A. ; ALLEN, J.E.: In: *Nuovo Cimento* 34 (1964), 529 S.

[25] FRY, W. F. ; SCHNEPS, J. ; SNOW, G. A. ; SWAMI, M. S.: Nuclear Capture of Negative K Mesons in Emulsion. In: *Phys. Rev.* 100 (1955), Dec, Nr. 5, S. 1448–1455. `http://dx.doi.org/10.1103/PhysRev.100.1448`. – DOI 10.1103/PhysRev.100.1448

[26] NIKOLIC, Milan M.: Hypernuclei produced by K- interactions in nuclear emulsions (I) mesic decays. In: *Nuclear Physics* 21 (1960), 595 - 598. `http://dx.doi.`

`org/DOI:10.1016/0029-5582(60)90080-8.` – DOI DOI: 10.1016/0029–5582(60)90080–8. – ISSN 0029–5582

[27] GEORGÃ©, V. ; KOCH, W. ; LINDT, W. ; NIKOLIC, M. ; SUBOTIC-NIKOLIC, S. ; WINZELER, H.: Hypernuclei produced by K- interactions in nuclear emulsions (II) general characteristics and non-mesic decays. In: *Nuclear Physics* 21 (1960), 599 - 623. `http://dx.doi.org/DOI:10.1016/0029-5582(60)90081-X.` – DOI DOI: 10.1016/0029–5582(60)90081–X. – ISSN 0029–5582

[28] TIETGE, J.: Eine systematische untersuchung π–mesonisch zerfallender hyperfragmente, die durch K^--mesonen erzeugt wurden. In: *Nuclear Physics* 20 (1960), 227 - 253. `http://dx.doi.org/DOI:10.1016/0029-5582(60)90172-3.` – DOI DOI: 10.1016/0029–5582(60)90172–3. – ISSN 0029–5582

[29] AMMAR, R. G. ; SETTI, R. L. ; SLATER, W. E. ; LIMENTANI, S. ; SCHLEIN, P. E. ; ; STEINBERG, P. H.: Mesic decays of hypernuclei from K^--capture II. Branching ratios in the charged mesic decay modes of $^3_\Lambda$H, $^4_\Lambda$H, $^4_\Lambda$He and $^5_\Lambda$He. In: *Nuovo Cimento* 19 (1961), Nr. 1, S. 20–35

[30] SCHLEIN, P.E. ; SLATER, W.E.: Identification of Heavy Hypernuclei from K^- Capture by Primary Star Analysis. In: *Nuovo Cimento* 21 (1961), Nr. 2, S. 213

[31] JONES, B. D. ; SANJEEVAIAH, B. ; ZAKRZEWSKI, J. ; CSEJTHEY-BARTH, M. ; LAGNAUX, J. B. ; SACTON, J. ; BENISTON, M. J. ; BURHOP, E. H. S. ; DAVIS, D. H.: Production of Hyperfragments from the Interactions of 800-MeV/c $K-$ Mesons with Emulsion Nuclei. In: *Phys. Rev.* 127 (1962), Jul, Nr. 1, S. 236–239. `http://dx.doi.org/10.1103/PhysRev.127.236.` – DOI 10.1103/PhysRev.127.236

[32] HENROTIN, H. ; LEMONNE, J. ; SACTON, J. ; DAVIS, D. H. ; SHAUKAT, M. A. ; ALLEN, J. E. ; KASIM, M. M.: The production of hyperfragments by the interactions in flight of low energy K- mesons with emulsion nuclei. In: *Physics Letters* 15 (1965), Nr. 2, 193 - 196. `http://dx.doi.org/DOI:10.1016/0031-9163(65)91337-5.` – DOI DOI: 10.1016/0031–9163(65)91337–5. – ISSN 0031–9163

[33] ABRAHAM, F. ; BENISTON, M. ; SETTI, R. L. ; VOSSLER, C. ; LEMONNE, J. ; SAC-
TON, J. ; BREIVIK, F.O. ; EIDE, Ã...J. ; FRODESEN, A.G. ; SKJEGGESTAD, O. ; UN-
NELAND, B.: Energy spectrum of charged pions from K- captures in CF3Br. In: *Nu-
clear Physics* 81 (1966), Nr. 2, 609 - 619. http://dx.doi.org/DOI:10.1016/
S0029-5582(66)80046-9. – DOI DOI: 10.1016/S0029–5582(66)80046–9. – ISSN
0029–5582

[34] CRAYTON, N. ; SETTI, R. L. ; RAYMUND, M. ; SKJEGGESTAD, O. ; ABELEDO, D.
; AMMAR, R. G. ; ROBERTS, J. H. ; SHIPLEY, E. N.: Compilation of Hyperfragment
Binding Energies. In: *Rev. Mod. Phys.* 34 (1962), Apr, Nr. 2, S. 186–189. http://dx.
doi.org/10.1103/RevModPhys.34.186. – DOI 10.1103/RevModPhys.34.186

[35] PROWSE, D. J.: An example of an N^{14} hyperfragment. In: *Physics Letters* 1 (1962),
Nr. 5, 178 - 180. http://dx.doi.org/DOI:10.1016/0031-9163(62)
90343-8. – DOI DOI: 10.1016/0031–9163(62)90343–8. – ISSN 0031–9163

[36] BHOWMIK, B.: The production and decay of a C^{14}-hyperfragment. In: *Physics
Letters* 2 (1962), Nr. 5, 220 - 222. http://dx.doi.org/DOI:10.1016/
0031-9163(62)90234-2. – DOI DOI: 10.1016/0031–9163(62)90234–2. – ISSN
0031–9163

[37] BHOWMIK, B. ; GOYAL, D.P. ; YAMDAGNI, N.K.: Binding energies of the Λ^0-hyperon in
hypernuclei. In: *Nuclear Physics* 40 (1963), 457 - 462. http://dx.doi.org/DOI:
10.1016/0029-5582(63)90288-8. – DOI DOI: 10.1016/0029–5582(63)90288–
8. – ISSN 0029–5582

[38] ANSELM ESSER: Observation of $^{4}_{\Lambda}Z$ Hyperhydrogen by Decay-Pion Spectroscopy in
Electron Scattering. In: *Physical Review Letters* (2015)

[39] AMMAR, R.G. ; CHOY, L. ; DUNN, W. ; HOLLAND, M. ; ROBERTS, J.H. ; SHIPLEY,
E.N. ; CRAYTON, N. ; DAVIS, D.H. ; LEVI-SETTI, R. ; RAYMUND, M. ; SKJEGGESTAD,
O. ; TOMASINI, G.: Binding Energies of Hypernuclei with Mass Number A>5. In:
Nuovo Cimento 26 (1963), S. 1078

[40] BOHM, G. ; KLABUHN, J. ; KRECKER, U. ; WYSOTZKI, F. ; COREMANS-BERTRAND, G. ; SACTON, J. ; VILAIN, P. ; WICKENS, J. H. ; WILQUET, G. ; STANLEY, D. ; DAVIS, D. H. ; ALLEN, J. E. ; PNIEWSKI, J. ; PNIEWSKI, T. ; ZAKRZEWSKI, J.: Evidence for the existence of particle-unstable states of the $^{12}_{\Lambda}$C and $^{14}_{\Lambda}$N hypernuclei. In: *Nuclear Physics B* 24 (1970), Nr. 2, 248 - 252. `http://dx.doi.org/DOI:10.1016/0550-3213(70)90235-X`. – DOI DOI: 10.1016/0550–3213(70)90235–X. – ISSN 0550–3213

[41] JURIC, M. ; BOHM, G. ; KRECKER, U. ; COREMANS-BERTRAND, G. ; SACTON, J. ; CANTWELL, T. ; MORIARTY, P. ; MONTWILL, A. ; DAVIS, D. H. ; KIELCZEWSKA, D. ; TYMIENIECKA, T. ; ZAKRZEWSKI, J.: Confirmation of the existence of a particle-unstable state of the [Lambda]12C hypernucleus. In: *Nuclear Physics B* 47 (1972), Nr. 1, 36 - 42. `http://dx.doi.org/DOI:10.1016/0550-3213(72)90098-3`. – DOI DOI: 10.1016/0550–3213(72)90098–3. – ISSN 0550–3213

[42] YAMADA, T. ; IKEDA, K.: In: *Phys. Rev. C* 56 (1997), 3216 S.

[43] HIRATA, Yuichi ; NARA, Yasushi ; OHNISHI, Akira ; HARADA, Toru ; RANDRUP, Jorgen: In: *Nucl. Phys. A* 639 (1998), 389c S.

[44] HIRATA, Yuichi ; NARA, Yasushi ; OHNISHI, Akira ; HARADA, Toru ; RANDRUP, JÃ¸rgen: In: *Prog. Theor. Phys.* 102 (1999), 89 S.

[45] BATTY, C. J. ; FRIEDMAN, E. ; GAL, A.: In: *Phys. Rev. C* 59 (1999), 295 S.

[46] NARA, Y. ; OHNISHI, A. ; HARADA, T. ; SHINMURA, S.: In: T.K.KOMATSUBARA, T.Shibata (Hrsg.) ; T.NOMURA (Hrsg.): *Proc. of the 25th INS International Symposium on Nuclear and Particle Physics with High-Intensity Proton Accelerators, Tokyo, Japan, Dec. 3-6, 1996*, World Scientific, Singapore, 1998, S. 324

[47] OHNISHI, A. ; HIRATA, Y. ; NARA, Y. ; SHINMURA, S. ; AKAISHI, Y.: In: *Nucl. Phys. A* 684 (2001), 595 S.

[48] BROWN, H.N. u. a.: In: *Phys. Rev. Lett.* 8 (1962), 255 S.

[49] DANYSZ, M. ; GARBOWSKA, K. ; PNIEWSKI, J. ; PNIEWSKI, T. ; ZAKRZEWSKI, J. ; FLETCHER, E. R. ; LEMONNE, J. ; RENARD, P. ; SACTON, J. ; TONER, W. T. ; O'SULLIVAN, D. ; SHAH, T. P. ; THOMPSON, A. ; ALLEN, P. ; HEERAN, M. ; MONTWILL, A. ; ALLEN, J. E. ; BENISTON, M. J. ; DAVIS, D. H. ; GARBUTT, D. A. ; BULL, V. A. ; KUMAR, R. C. ; ; MARCH, P. V.: Observation of a Double Hyperfragment. In: *Nucl. Phys.* 49 (1963), S. 121

[50] PROWSE, D.J.: In: *Phys. Rev. Lett* 17 (1966), 782 S.

[51] DALITZ, R.H. ; DAVIS, D.H. ; FOWLER, P.H. ; MONTWILL, A. ; PNIEWSKI, J. ; ZAKRZEWSKI, J.A.: In: *Proc. R. Soc. Lond. A* 426 (1989), 1 S.

[52] DOVER, C.B. ; MILLENER, D.J. ; GAL, A. ; DAVIS, D.H.: In: *Phys. Rev. C* 44 (1991), 1905 S.

[53] AOKI, S. u. a.: In: *Prog. Theor. Phys.* 85 (1991), 1287 S.

[54] TAKAHASHI, H. ; AHN, J.K. ; AKIKAWA, H. ; AOKI, S. ; ARAI, K. ; BAHK, S.Y. ; BAIK, K.M. ; BASSALLECK, B. ; CHUNG, J.H. ; CHUNG, M. S. ; DAVIS, D. H. ; FUKUDA, T. ; HOSHINO, K. ; ICHIKAWA, A. ; IEIRI, M. ; IMAI, K. ; IWATA, Y.H. ; IWATA, Y.S. ; KANDA, H. ; KANEKO, M. ; KAWAI, T. ; KAWASAKI, M. ; KIM, C.O. ; KIM, J.Y. ; KIM, S.J. ; KIM, S.H. ; KONDO, Y. ; KOUKETSU, T. ; LEE, Y. L. ; MCNABB, J.W.C. ; MITSUHARA, M. ; NAGASE, Y. ; NAGOSHI, C. ; NAKAZAWA, K. ; NOUMI, H. ; OGAWA, S. ; OKABE, H. ; OYAMA, K. ; PARK, H.M. ; PARK, I.G. ; PARKER, J. ; RA, Y.S. ; RHEE, J.T. ; RUSEK, A. ; SHIBUYA, H. ; K.S. SIM, P.K. S. ; SEKI, D. ; SEKIMOTO, M. ; SONG, J. S. ; TAKAHASHI, T. ; TAKEUTCHI, F. ; TANAKA, H. ; TANIDA, K. ; TOJO, J. ; TORII, H. ; TORIKAI, S. ; TOVEE, D. N. ; USHIDA, N. ; YAMAMOTO, K. ; YASUDA, N. ; YANG, J.T. ; YOON, C.J. ; YOON, C.S. ; YOSOI, M. ; YOSHIDA, T. ; ZHU, L.: In: *Phys. Rev. Lett.* 87 (2001), 212501–1 S.

[55] TANIDA, K. u. a.: Plan for the measurement of Ξ^--atomic X rays at J-PARC. In: POCHODZALLA, J. (Hrsg.) ; WALCHER, Th. (Hrsg.): *Proc. of the IX International Con-*

ference on Hypernuclear and Strange Particle Physics, SIF and Springer-Verlag Berlin Heidelberg, 2007, S. 145

[56] YAMADA, T. ; NAKAMOTO, C.: In: *Phys. Rev. C* 62 (2000), 034319–1 S.

[57] HIYAMA, E. u. a.: In: *Phys. Rev. C* 66 (2002), 024007 S.

[58] AHN, J. K. ; AJIMURA, S. ; AKIKAWA, H. ; BASSALLECK, B. ; BERDOZ, A. ; CARMAN, D. ; CHRIEN, R. E. ; DAVIS, C. A. ; EUGENIO, P. ; FISCHER, H. ; FRANKLIN, G. B. ; FRANZ, J. ; FUKUDA, T. ; GAN, L. ; HOTCHI, H. ; ICHIKAWA, A. ; IMAI, K. ; KAHANA, S. H. ; KHAUSTOV, P. ; KISHIMOTO, T. ; KORAN, P. ; KOHRI, H. ; KOUREPIN, A. ; KUBOTA, K. ; LANDRY, M. ; MAY, M. ; MEYER, C. ; MEZIANI, Z. ; MINAMI, S. ; MIYACHI, T. ; NAGAE, T. ; NAKANO, J. ; OUTA, H. ; PASCHKE, K. ; PILE, P. ; PROKHABATILOV, M. ; QUINN, B. P. ; RASIN, V. ; RUSEK, A. ; SCHMITT, H. ; SCHUMACHER, R. A. ; SEKIMOTO, M. ; SHILEEV, K. ; SHIMIZU, Y. ; SUTTER, R. ; TAMAGAWA, T. ; TANG, L. ; TANIDA, K. ; YAMAMOTO, K. ; YUAN, L.: Production of $^{4}_{\Lambda\Lambda}H$ Hypernuclei. In: *Phys. Rev. Lett.* 87 (2001), Sep, 132504. `http://dx.doi.org/10.1103/PhysRevLett.87.132504`. – DOI 10.1103/PhysRevLett.87.132504

[59] RANDENIYA, S. D. ; HUNGERFORD, E. V.: Reevaluation of the reported observation of the $_{\Lambda\Lambda}{}^{4}$H hypernucleus. In: *Phys. Rev. C* 76 (2007), Dec, 064308. `http://dx.doi.org/10.1103/PhysRevC.76.064308`. – DOI 10.1103/PhysRevC.76.064308

[60] FAIR: *Understanding the creation of mass-the PANDA experiment at FAIR.* `http://www.fair-center.eu/public/experiment-program/antiproton-physics/panda.html`, 2015

[61] J. POCHODZALLA, A. BOTVINA, A. SANCHEZ LORENTE: Studies of Hyperons and Antihyperons in Nuclei. In: *Proceedings of Science* (2010)

[62] PANDA COLLABORATION: *The PANDA Detector - Overview.* `https://panda.gsi.de/oldwww/framework/detector.php`,

[63] F. FERRO, F. I. M. Agnello A. M. Agnello ; SZYMANSKA, K.: Cascades minus production in antiproton-nucleus collisions at 3 GeV/c. In: *Science Direct* (2007)

[64] BUSS, O. ; GAITANOS, T. ; GALLMEISTER, K. ; HEES, H. van ; KASKULOV, M. ; LALAKULICH, O. ; LARIONOV, A.B. ; LEITNER, T. ; WEIL, J. ; MOSEL, U.: Transport-theoretical description of nuclear reactions. In: *Physics Reports* 512 (2012), Nr. 1-2, 1 - 124. http://dx.doi.org/http://dx.doi.org/10.1016/j.physrep. 2011.12.001. – DOI http://dx.doi.org/10.1016/j.physrep.2011.12.001. – ISSN 0370–1573. – Transport-theoretical Description of Nuclear Reactions

[65] SEBASTIAN BLESER: *The target system for the hypernuclear experiment at $\overline{P}ANDA$*, Johannes Gutenberg-Universität Mainz, Diss., 2016. – in preparation

[66] LEHRACH, A. ; BOINE-FRANKENHEIM, O. ; HINTERBERGER, F. ; MAIER, R. ; PRASUHN, D.: Beam performance and luminosity limitations in the high-energy storage ring (HESR). In: *Nuclear Instruments and Methods in Physics Research Section A: Accelerators, Spectrometers, Detectors and Associated Equipment* 561 (2006), Nr. 2, 289 - 296. http://dx.doi.org/http://dx.doi.org/10.1016/j.nima. 2006.01.017. – DOI http://dx.doi.org/10.1016/j.nima.2006.01.017. – ISSN 0168–9002. – Proceedings of the Workshop on High Intensity Beam DynamicsCOULOMB 2005Workshop on High Intensity Beam Dynamics

[67] SEBASTIAN BLESER: *Primary target.* 2013. – $\overline{P}$ANDA Meeting

[68] MITSUBISHI RAYON CO.,LTD: *Pitch-based Carbon Fiber(CF) DIALEAD.* https://www.mrc.co.jp/dialead/english/dialead.html, 2015

[69] DIAMOND MATERIALS: *Thermal properties of diamond.* http://www.diamond-materials.com/EN/cvd_diamond/thermal_properties.htm, 2015

[70] WIKIPEDIA FOUNDATION: *Silicon.* https://en.wikipedia.org/wiki/Silicon, 2015

[71] WIKIPEDIA FOUNDATION: *Titanium.* https://en.wikipedia.org/wiki/Titanium, 2015

[72] WIKIPEDIA FOUNDATION: *Copper.* https://en.wikipedia.org/wiki/Copper, 2015

[73] INSTITUT FÜR KERNPHYSIK, MAINZ: *The Mainz Microtron.* http://www.kph.uni-mainz.de/eng/108.php,

[74] NATIONAL INSTITUTE OF STANDARDS AND TECHNOLOGY: *ESTAR stopping power and range tables for electrons.* http://physics.nist.gov/PhysRefData/Star/Text/ESTAR.html, 2015

[75] K.A.OLIVE ET AL.: *Particle Data Group, Ξ^- Baryon.* pdg.lbl.gov/2015/listings/rpp2015-list-xi-minus.pdf, 2014

[76] SEBASTIAN BLESER: *Status of the target system for the hypernuclear experiment.* 2015. – $\overline{\text{P}}$ANDA Meeting

[77] PABLO GOMIS AND MIGUEL ESCUDERO: *Primary target developments for the Hypernuclei experiment at PANDA.* 2014

[78] PIEZOMOTOR: *PiezoWave Linear 0.1 N*, 2015

[79] NANOMOTION LTD.: *HR1 Ultrasonic Motor User Manual*, 2008

[80] MICROE SYSTEMS: *Mercury 1000V - Vacuum Rated Analog Encoder. Reflective Linear and Rotary Vacuum Encoders*, 2015

[81] PIEZOMOTOR: *PiezoWave Demokit Preliminary Data 20060601*, 2015

[82] PFEIFFER VACUUM: *Turbomolecular pumps, Design/Operating principle.* https://www.pfeiffer-vacuum.com/en/know-how/vacuum-generation/turbomolecular-pumps/,

[83] VACOM: *Ion Getter and Titanium Sublimation Pumps, Vacuum creation with ion getter pumps.* `http://www.vacom.de/en/products/ion-getter-and-titanium-sublimation-pumps`,

[84] OERLIKON, LEYBOLD VACUUM: *Scroll Vacuum Pumps.* `https://leyboldproducts.oerlikon.com/us/us/produktkatalog_03.aspx?cid=20_30_0`,

[85] STANFORD RESEARCH SYSTEMS: *Operating Manual and Programming Reference, Models RGA100, RGA200, and RGA300 Residual Gas Analyzer.* `http://www.thinksrs.com/downloads/PDFs/Manuals/RGAm.pdf`, 2009

[86] MICROE SYSTEMS: *Mercury 1000V - Vacuum Rated Analog Output Encoder System. Installation Manual and Reference Guide*, 2008

[87] NANOMOTION LTD.: *AB1A Driver User Manual*, 2008

[88] PIEZOMOTOR: *Piezo LEGS Linear 6N LL10, Specifications.* `http://www.piezomotor.com/products/linear/ll10/`, 2015

[89] FABIAN NILLIUS: *Private Comunication.* 2014